

AD-A172 754

INTERACTION BETWEEN WATER BORNE WAVES AND SEISMIC WAVES

1/2

IN THE OCEAN BOTTOM (U) NORWEGIAN DEFENCE RESEARCH

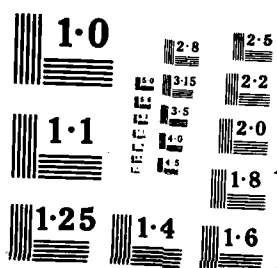
ESTABLISHMENT KJELLER J GLATTEIRE 15 APR 86

UNCLASSIFIED

NDRE/PUBL-86/1001

F/G 28/1

NL



AD-A172 754

INTERACTION BETWEEN WATER BORNE WAVES
AND SEISMIC WAVES IN THE OCEAN BOTTOM:
THE FORWARD- AND INVERSE PROBLEM

BY
J GLATTETRE

DTIC
SELECTE
OCT 06 1986
S D

NDRE PUBLICATION-86/1001

DTIC FILE COPY

FORSVARETS FORSKNINGSinSTITUTT

NORWEGIAN DEFENCE RESEARCH ESTABLISHMENT

P O Box 25 - N-2007 Kjeller, Norway

This document has been approved
for public release and sale; its
distribution is unlimited.

142120PTM

86 10 6 033

DISCLAIMER NOTICE

**THIS DOCUMENT IS BEST QUALITY
PRACTICABLE. THE COPY FURNISHED
TO DTIC CONTAINED A SIGNIFICANT
NUMBER OF PAGES WHICH DO NOT
REPRODUCE LEGIBLY.**

**INTERACTION BETWEEN WATER BORNE WAVES AND SEISMIC
WAVES IN THE OCEAN BOTTOM: THE FORWARD- AND INVERSE
PROBLEM**

by

J GLATTETRE

NDRE PUBLICATION-86/1001

FORSVARETS FORSKNING SINSTITUTT

NORWEGIAN DEFENCE RESEARCH ESTABLISHMENT

P O Box 25 - N-2007 Kjeller, Norway

April 1986

NORWEGIAN DEFENCE RESEARCH ESTABLISHMENT (NDRE)
FORSVARETS FORSKNINGINSTITUTT (FFI)

UNCLASSIFIED

POST OFFICE BOX 25
N-2007 KJELLER, NORWAY

SECURITY CLASSIFICATION OF THIS PAGE
(when data entered)

REPORT DOCUMENTATION PAGE

1) PUBL/REPORT NUMBER NDRE/PUBL-86/1001 1a) JOB REFERENCE	2) SECURITY CLASSIFICATION UNCLASSIFIED 2a) DECLASSIFICATION/DOWNGRADING SCHEDULE	3) NUMBER OF PAGES 103
4) TITLE INTERACTION BETWEEN WATER BORNE WAVES AND SEISMIC WAVES IN THE OCEAN MOTTOM: THE FORWARD- AND INVERSE PROBLEM		
5) NAMES OF AUTHOR(S) IN FULL (surname first) GLATTETRE John		
6) DISTRIBUTION STATEMENT Approved for public release. Distribution unlimited (Offentlig tilgjengelig)		
7) INDEXING TERMS		
IN ENGLISH:		IN NORWEGIAN:
a) <u>Shallow water</u>	a) <u>Grunnt vann</u>	
b) <u>Underwater acoustics</u>	b) <u>Undervannsakustikk</u>	
c) <u>Seismic waves</u>	c) <u>Seismiske bølger</u>	
d) <u>Mathematical models</u>	d) <u>Matematiske modeller</u>	
e) _____	e) _____	
8) ABSTRACT REFERENCE. Thesaurus of Engineering and Scientific terms		
8) ABSTRACT (continue on reverse side if necessary)		
<p>The work is divided into two main parts. The first part, the forward problem, is aimed at establishing a theoretical framework for excitation and propagation of elastic waves in linear homogeneous isotropic media.</p> <p>The second part, the inverse problem, is aimed at determining the environmental parameters which significantly influence acoustic propagation in a shallow water environment.</p> <p>The methods developed here indicate that, under favorable conditions, it is possible to infer ocean bottom parameters such as P- and S- wave phase velocities from near surface measurements.</p>		
9) DATE 15 April 1986	AUTHORIZED BY This page only E Klippenberg	POSITION Director

UNCLASSIFIED

SECURITY CLASSIFICATION OF THIS PAGE
(when data entered)

SECURITY CLASSIFICATION OF THIS PAGE
(when data entered)

ABSTRACT (continued)

SECURITY CLASSIFICATION OF THIS PAGE
(when data entered)

CONTENTS	PAGE
SUMMARY	4
1 INTRODUCTION	5
2 THE FORWARD PROBLEM	6
2.1 Introduction	6
2.2 List of symbols	9
2.3 The homogeneous solution	11
2.4 Source field	25
2.5 Solution technique	27
2.5.1 Numerical integration of the Bessel transform	27
2.5.2 The global matrix method	29
2.5.3 Numerical considerations	33
2.6 Numerical example: a point source in free space	35
3 THE INVERSE PROBLEM	36
3.1 Introduction	36
3.2 Some basic properties of a monolayer waveguide	38
3.3 A test case	40
3.3.1 The 0. mode	42
3.3.2 The higher order modes	44
3.4 Description of data collection and system response	47
3.5 Preprocessing and display of measured data	49
3.6 Modelling of the data collection system	50
3.7 Geoaoustical background information	52
3.8 Identification- and modelling of events in the measured data	54
3.8.1 First approximation	54
3.8.2 Second approximation	59
3.9 Discussion of fit between measurement and model	64
3.10 Suggestions for future work	66
4 CONCLUSIONS	67
5 ACKNOWLEDGEMENTS	68
6 REFERENCES	69
Appendix 1: Rayleigh- pseudo- Rayleigh and Scholte waves	71
Appendix 2: Geoaoustical properties of various sediment and rock types	72



IV	
D. L. L. L. L.	
Availability Codes	
Availability Codes	
23	23

INTERACTION BETWEEN WATER BORNE WAVES AND SEISMIC WAVES IN THE OCEAN
BOTTOM: THE FORWARD- AND INVERSE PROBLEM.

ABSTRACT

The work is divided into two main parts. The first part, the forward problem, is aimed at establishing a theoretical framework for excitation and propagation of elastic waves in linear homogeneous isotropic media.

The second part, the inverse problem, is aimed at determining the environmental parameters which significantly influence acoustic propagation in a shallow water environment.

The methods developed here indicate that, under favorable conditions, it is possible to infer ocean bottom parameters such as P- and S- wave phase velocities from near surface measurements.

1 INTRODUCTION

The work reported here is a partial fulfillment of the requirements for the degree Dr Ing under the supervision of professor Jens Hovem at the University of Trondheim, the Norwegian Institute of Technology.

The work is divided into two main parts. The first part, the forward problem, is aimed at establishing a theoretical framework for excitation and propagation of elastic waves in linear homogeneous isotropic media. As the solution is limited to horizontally stratified media, a separable solution of the equation of motion is derived.

In the outset, a numerical solution was implemented based on the Thomson-Haskell matrix method[3,4] as derived by Kutschale[7]. This approach was later abandoned and a two-dimensional model - developed at the SACLANT ASW Research centre at LaSpezia, Italy by Henrik Schmidt [9] - was modified to the present three-dimensional version.

The second part, the inverse problem, is aimed at determining the environmental parameters that significantly influence acoustic propagation in a shallow water environment. This is done by interpreting shot data gathered by a seismic survey. Interpretation is sought verified by comparison with output from the numerical model. To my knowledge, the inverse problem methods utilized here have not been published earlier.

2 THE FORWARD PROBLEM

2.1 Introduction

It is well known that separable solutions lead to the use of integral transform techniques which yield an exact solution to the wave equation in stratified elastic media[1]. The field parameters are, however, determined by linear combinations of the basis for the solution space i.e. inverse transform integrals. In cases with only a few layers, contour integration can be used to reduce the numerical computation, involving only a few integrations over finite intervals, e.g. [1]. In general numerical models, however, such techniques are inconvenient, and direct numerical integration has to be used.

In underwater acoustics in general, and also for the cases we will investigate here, the sources are usually contained within a volume small compared to the volume of interest, thus the radiated field is most conveniently described in a cylindrical coordinate system. The field is then given by Hankel transform integrals which are not well suited for direct numerical integration due to the Bessel functions involved. In order to overcome this problem, Marsh[2] in 1961 introduced what was later called the fast field approximation (FFP = Fast Field Program) of the Hankel transform. The field is separated into ingoing and outgoing parts by expressing the Bessel function in terms of Hankel functions, the ingoing part is disregarded and the outgoing part is replaced by its large argument approximations. The integrals are then evaluated by means of the fast Fourier transform (FFT). As shown later by DiNapoli and Deavenport[5], for the two-dimensional case, the fast field approximation gives no significant errors at ranges longer than a few wavelengths from the axis.

After the introduction of the fast field technique, a number of numerical models have been developed, based on this integration method and thus usually called fast field programs.

In spite of their common name, these models are significantly different, especially concerning the approach taken to solve the transformed wave equations in a multilayered environment. Traditionally, the depth dependence of the field has been determined by means of the Thomson-Haskell matrix method[3,4]. The first model was introduced by DiNapoli[6], who evaluated the solution very efficiently by means of recurrence relations for the hypergeometric functions. However this approach allows only for fluid layers, and in that case, other techniques, like normal mode methods, are usually more convenient. The first FFP model, including the coupling between compressional and vertical shear waves at the boundaries of solid layers, was developed by Kutschale[7] also using the Thomson-Haskell method. The original model allowed for only one source/receiver combination for each solution. It has later been modified by Harrison[8] to allow for several receivers, but even for one combination the computations are rather extensive.

A more direct and computationally more efficient solution technique was recently introduced by Schmidt[9]. The field parameters at the interfaces are expressed in terms of source contributions and unknown scalar potentials. The boundary conditions yield a system of equations in the Hankel transforms of the potentials to be satisfied at each interface. These local systems of equations are mapped into a global set of equations using a technique similar to the one used in finite element programs. The computational speed has been improved by an order of magnitude by use of this solution technique. Furthermore configurations involving several sources and/or receivers can be treated with one solution, thus yielding the possibility of computing total fields generated not only by single point sources, but also by vertical source arrays.

These and similar models have all been two-dimensional, thus restricting the sources to be placed on the axis of the cylindrical coordinate system. A direct solution of problems with horizontally distributed sources has therefore not been possible, but has required a new calculation for each source and subsequent superposition. In this paper the model of Schmidt[9] has been modified and extended to allow for sources displaced with respect to the axis.

The field parameters are expanded in a Fourier series in the angular direction, thus leading to an infinite number of two-dimensional problems. By expressing the boundary conditions in terms of Cartesian components, rather than polar components, the coefficient matrix will be independent of the Fourier order, and the Hankel transforms of all the expansion coefficients for the unknown potentials can be found with only one matrix inversion for each horizontal wavenumber. The truncation point of the Fourier series can be determined a priori.

The inversion of the Hankel transforms is again performed by means of the fast field technique, and the angular distribution is evaluated from the expansion coefficients by means of an FFT technique.

In the following the model and its mathematical background will be described.

2.2 List of symbols

ω	angular frequency
λ	Lame' constant and wavelength
μ	Lame' constant
ρ	density
c_c	compressional wave phase velocity
c_s	shear wave phase velocity
ϕ	compressional wave potential
ψ	shear wave potential
Λ	shear wave potential
$\vec{\Omega}$	shear wave potential vector
\vec{U}	particle displacement vector
u_1	particle displacement in 1-direction
\vec{V}	particle displacement velocity vector
v_1	particle displacement velocity in 1-direction
T_{1k}	stress in direction 1 applied to surface with normal vector k
S_{1k}	strain in direction 1 of surface with normal vector k
c_{iklm}	stiffness constants
δ_{1k}	Kronecker delta
$\delta(x)$	Dirac delta "function"
$J_1(z)$	Bessel function of first kind, order 1
$N_1(z)$	Neumann function of order 1
$H_1^{(2)}(z)$	Hankel function of second kind, order 1
k	horizontal wave number
α	vertical wave number for compressional waves

β vertical wavenumber for shear waves
 \sim tilde: denotes source terms
 F_n^m vector of parameters entering boundary conditions in
 layer n for angular order m
 B_n^m vector of up- and downward- going potentials in layer
 n for angular order m
 $A_{n,i}$ matrix relating B_n^m to F_n^m in layer n , $i=1$: lower
 $i=u$: upper
 R_n^m source contributions in layer n , angular order m

2.3 The homogeneous solution

The solution will be restricted to a homogeneous medium, hence the environmental parameters are independent of spatial position.

Newtons second law of motion for a solid may be stated in a frame of Cartesian coordinates using tensor notation as

$$\frac{\partial T_{ik}(x_x, x_y, x_z)}{\partial x_k} = \rho \frac{\partial^2 u_i(x_x, x_y, x_z)}{\partial t^2} \quad (1)$$

The subscripts take on values from 1 to 3 indicating directions x, y and z respectively. Einstein's summation convention i.e. summation over identical indexes is assumed.

T_{ik} is the stress tensor: stress in direction i applied to surface with normal-vector k.

u_i is particle displacement in i-direction.

The spatial arguments of T and u will in the following be omitted, but assumed tacitly.

ρ is the density of the medium.

(1) thus equates the force in direction i applied to an infinitesimal volume element to its inertia in direction i.

As the only forces acting on the volume element are the internal volume forces, the volume is considered source-free.

The medium described by (1) is furthermore lossless. Viscous losses can be included by entering a first order time derivative term. A discussion on the causality of time-dependent solutions when entering losses is given in [17].

The linear elastic material properties for a general solid may be stated as

$$T_{ik} = c_{iklm} S_{lm} \quad (2)$$

which is Hooke's law. The deformation is

$$S_{lm} = \frac{1}{2} \left[\frac{\partial u_l}{\partial x_m} + \frac{\partial u_m}{\partial x_l} \right] \quad (3)$$

We have the following symmetry relations

$$T_{ik} = T_{ki} \quad (4a)$$

$$S_{lm} = S_{ml} \quad (4b)$$

$$c_{iklm} = c_{kilm} = c_{ikml} = c_{lmik} \quad (4c)$$

(4a) follows as a consequence of the torsional moment vanishing at equilibrium [16]. (4b) is an obvious consequence of (3). The three first terms of (4c) are consequences of (4a) and (4b) respectively, while the fourth term follows from thermodynamical considerations [16].

Thus, c_{iklm} has at most 21 independent components.

For c_{iklm} to be isotropic, it is required that [14]

$$c_{iklm} = \lambda \delta_{ik} \delta_{lm} + \mu \delta_{il} \delta_{km} + \nu \delta_{im} \delta_{kl} \quad (5)$$

(4a) implies that $\mu = \nu$ since $c_{iklm} = c_{kilm}$.

The constitutive relation for an isotropic solid is thus simplified to be

$$T_{ik} = \delta_{ik} \lambda \frac{\partial u_l}{\partial x_l} + \mu \left[\frac{\partial u_i}{\partial x_k} + \frac{\partial u_k}{\partial x_i} \right] \quad (6)$$

which rewritten in ∇ -operator notation is

$$T_{ik} = \delta_{ik} \lambda \nabla \cdot \vec{u} + 2 \mu S_{ik} \quad (7)$$

The first two symmetry properties given in (4) state that both T_{ik} and S_{ik} are symmetric. If they furthermore are real, they may be written as real symmetric matrixes which consequently are selfadjoint. Diagonalization gives the stress and strain respectively along what is termed the principal axes. Then [15]

$$T_n = \lambda \nabla \cdot U + 2 \mu S_n \quad (8)$$

This form is valuable for giving insight into the physical interpretation of the Lamé constants. For a fluid where $\mu=0$, λ becomes the bulk modulus. For a solid, the effect due to the principal stress T_n would be a dilatation plus an extension in the n -direction

It should be noted that the material constants which normally enter into our equations are the adiabatic terms as we assume that negligible heat is transferred to the medium.

In order to combine equations (1) and (6), (6) is differentiated with respect to x_k and the common term eliminated. The result, rewritten in ∇ -operator notation, becomes

$$(\lambda + \mu) \nabla \nabla \cdot \vec{U} + \mu \nabla^2 \vec{U} = \rho \frac{\partial^2 \vec{U}}{\partial t^2} \quad (9)$$

Use of the vector identity

$$\nabla \times \nabla \times \vec{A} = \nabla \nabla \cdot \vec{A} - \nabla^2 \vec{A} \quad (10)$$

enables us to bring (9) to a commonly used form termed the equation of motion for a solid isotropic homogenous lossless medium containing no sources

$$c_c^2 \nabla \nabla \cdot \vec{U} - c_s^2 \nabla \times \nabla \times \vec{U} - \frac{\partial^2 \vec{U}}{\partial t^2} = \vec{0} \quad (11)$$

where the phase velocities for compressional- and shear waves are

$$c_c^2 = \frac{\lambda + 2\mu}{\rho} \quad (12a)$$

$$c_s^2 = \frac{\mu}{\rho} \quad (12b)$$

respectively.

The introduction of the wave velocities at this stage is an anticipation of things to come. It will be shown that these quantities are phase velocities and, indeed, phase velocities related to compressional- and shear-waves respectively.

Separating the solution of (11) into a space- and a time-dependent part, will imply a time-dependent part of the form $\exp(\pm j\omega t)$ of which

$\exp(j\omega t)$ is chosen. The symbol \vec{U} , up to now used to denote the time- and space-dependent particle movement, will in the following, unless otherwise stated, be taken to mean just the space-dependent part. This should not cause confusion. (11) is thus reduced to

$$c_c^2 \nabla \nabla \cdot \vec{U} - c_s^2 \nabla \times \nabla \times \vec{U} + \omega^2 \vec{U} = \vec{0} \quad (13)$$

A common approach for further reduction of (13) [12][13] is to express the solution as the sum of a longitudinal- and a transversal term i.e

$$\vec{U} = \vec{U}_T + \vec{U}_L \quad (14)$$

where

$$\nabla \cdot \vec{U}_T = 0 \quad (15a)$$

$$\nabla \times \vec{U}_L = 0 \quad (15b)$$

Insertion of (14), (15a) and (15b) into (13) yields

$$c_c^2 \nabla \nabla \cdot \vec{U}_L - c_s^2 \nabla \times \nabla \times \vec{U}_T + \omega^2 \vec{U} = \vec{0} \quad (16)$$

We define

$$\phi' = \nabla \cdot \vec{U}_L \quad (17a)$$

$$\vec{Q} = \nabla \times \vec{U}_T \quad (17b)$$

which inserted into (16) yields

$$\vec{U} = -\frac{c^2}{\omega^2} \nabla \cdot \phi' + \frac{c^2}{\omega^2} \nabla \times \vec{Q} \quad (18)$$

The vector quantity in the second term of (18) may be reduced to a scalar by expressing the potential vector as

$$\frac{\omega}{c_s} \vec{Q} = \vec{\Psi} \vec{a} + \nabla \times \vec{\Lambda} \vec{a} \quad (19)$$

where \vec{a} is a unit vector. It is common practice in z-dependent media, [3][4][7] to choose \vec{a} to be aligned with the z-axis. The displacement components arising from Ψ will not have components in the z-direction, thus representing a transversal shear wave which does not enter into the two-dimensional (range and depth) case.

The displacement may now be written

$$\vec{U} = \nabla \phi + \nabla \times \vec{\Psi} \vec{z} + \nabla \times \nabla \times \vec{\Lambda} \vec{z} \quad (20)$$

As (16) is a linear operator, here termed L, then

$$L(\vec{U}) = L(\nabla \phi + \nabla \times \vec{\Psi} \vec{z} + \nabla \times \nabla \times \vec{\Lambda} \vec{z}) = \vec{0} \quad (21)$$

is equivalent with

$$L(\nabla \phi) + L(\nabla \times \vec{\Psi} \vec{z}) + L(\nabla \times \nabla \times \vec{\Lambda} \vec{z}) = 0 \quad (22)$$

As the left hand side of (20) is obviously a vectorfunction of the three spatial directions, it may be decomposed into three linearly independent scalar functions. So must also than be the case with the right hand side of (20) as well, the three scalar functions ϕ, Ψ and Λ are linearly independent. As each term of (22) is linearly independent, they can at most be a constant. We will here in the following restrict our attention to assuming this constant to be zero. Thus, (22) is implied by

$$L(\nabla\phi) = 0 \quad (23a)$$

$$L(\nabla \times \vec{\Psi}) = 0 \quad (23b)$$

$$L(\nabla \times \nabla \times \vec{\Lambda}) = 0 \quad (23c)$$

thus (16) is satisfied if

$$\nabla(c_c^2 \nabla^2 \phi + \omega^2 \phi) = 0 \quad (24a)$$

$$\nabla \times (-c_s^2 \nabla \times \nabla \times \vec{\Psi} + \omega^2 \vec{\Psi}) = 0 \quad (24b)$$

$$\nabla \times \nabla \times (-c_s^2 \nabla \times \nabla \times \vec{\Lambda} + \omega^2 \vec{\Lambda}) = 0 \quad (24c)$$

The quantities within brackets of (24a) can at most be constant. As sources at infinity are discarded, the radiation condition imposes that $\phi \rightarrow 0$ when $|\vec{r}| \rightarrow \infty$, thus implying the bracketed term being 0. (24b) and (24c) are clearly fulfilled if the bracketed terms are constant. The same physical considerations as applied to (24a) are valid, thus yielding that the bracketed terms vanish when $|\vec{r}| \rightarrow \infty$.

Application of the vector identity (10) to the bracketed terms of (24b) and (24c) bring these two equations to being of the Helmholtz type and in summarizing: if (20) is a solution of (13), then

$$\nabla^2 \phi + h^2 \phi = 0 \quad (25a)$$

$$\nabla^2 \vec{\Psi} + g^2 \vec{\Psi} = 0 \quad (25b)$$

$$\nabla^2 \vec{\Lambda} + g^2 \vec{\Lambda} = 0 \quad (25c)$$

where h and g are the wavenumbers for compressional- and shear waves respectively:

$$h^2 = \frac{\omega^2}{c_c^2} = \frac{\rho \omega^2}{\lambda + 2\mu} \quad (26)$$

$$g^2 = \frac{\omega^2}{c_s^2} = \frac{\rho \omega^2}{\mu} \quad (27)$$

It has been stated (11), without being shown, that it is the compressional and shear wave velocities that enter into (9). A separable solution of (25) in a Cartesian coordinate system is

$$\theta(x,y,z) = e^{-j(k_x x + k_y y + k_z z)} \quad (28)$$

where

$$h^2 = k_x^2 + k_y^2 + k_z^2 \quad (29)$$

As all directions are equivalent, propagation in the x-direction may be considered with no loss of generality. Inclusion of the time-dependent factor yields

$$\phi(t,x) = e^{j(\omega t - k_x x)} \quad (30)$$

For constant phase the argument of the exponential function is constant, thus

$$\frac{x}{t} = \frac{\omega}{k_x} = \frac{\omega}{h} = \left(\frac{\lambda + 2\mu}{\rho} \right)^{1/2} = c_c \quad (31)$$

Similarly, a solution of (25b) and (25c) will yield

$$\frac{x}{t} = \frac{\omega}{k_x} = \left(\frac{\mu}{\rho} \right)^{1/2} = c_s \quad (32)$$

Application of (20) to (28) gives

$$\vec{U}_\phi = -jk_x e^{j(\omega t - k_x x)} \vec{x} \quad (33a)$$

$$\vec{U}_\psi = jk_x e^{j(\omega t - k_x x)} \vec{y} \quad (33b)$$

$$\vec{U}_\lambda = k_x^2 e^{j(\omega t - k_x x)} \vec{z} \quad (33c)$$

ϕ represents a wave propagating in x-direction with phase velocity c_c and with particle displacement in the direction of propagation, while ψ and Λ propagate in the same direction with phase velocity c_s but with particle displacements perpendicular to the propagation direction.

If $\vec{U}_n = \{u_{rn}, u_{\theta n}, u_{zn}\}$ are the displacement components referred to a cylindrical coordinate system $\{r, \theta, z\}$ in a homogeneous layer n , (13) will be satisfied for (20) expressed in cylindrical coordinates as

$$u_{rn} = \frac{\partial \phi_n}{\partial r} + \frac{1}{r} \frac{\partial \psi_n}{\partial \theta} + \frac{\partial^2 \Lambda_n}{\partial r \partial z} \quad (34)$$

$$u_{\theta n} = \frac{1}{r} \frac{\partial \phi_n}{\partial \theta} - \frac{\partial \psi_n}{\partial r} + \frac{1}{r} \frac{\partial^2 \Lambda_n}{\partial \theta \partial z} \quad (35)$$

$$u_{zn} = \frac{\partial \phi_n}{\partial z} - \left(\frac{1}{r} \frac{\partial}{\partial r} r \frac{\partial}{\partial r} + \frac{1}{r^2} \frac{\partial^2}{\partial \theta^2} \right) \Lambda_n \quad (36)$$

where the potentials satisfy the homogeneous scalar wave equations (25a), (25b) and (25c)

If a solution where there is no θ -dependence is examined, it is readily seen that both u_r and u_z are dependent upon both ϕ and Λ , while u_θ is dependent solely on ψ . Previous models [3][4] had separate uncoupled solutions for these two cases. The two-dimensional realization based on ϕ and Λ could support compressional-, shear in r and z plane- and surface-waves such as Rayleigh (vacuum-solid interface) Scholte (liquid-solid interface) and Stoneley (solid-solid interface). The one-dimensional realization was used to study transversal shear waves (displacement in θ -direction) and chiefly Love waves. These are transversal shear waves confined to a waveguide limited by two interfaces.

The attenuation in the medium can be accounted for by allowing the Lamé constants and thus also the wavenumbers to be complex. This follows from including viscous losses by adding a first order time-derivative term to (1). One must be aware when including losses in this manner and performing integration over frequency to obtain a time-dependent solution, the answer may come out non-causal. A

discussion of this problem is found in [17]. This point will, however, not be given more attention here.

In order not to confuse, the index n referring to the layer number will be implied in the rest of this section.

A set of solutions of equations (25) of the separable form

$$\Phi(r, \theta, z) = R(r) \Theta(\theta) Z(z) \quad (37)$$

is sought. This yields the separated ordinary differential equations

$$\Theta'' + m^2 \Theta = 0 \quad (38)$$

$$Z'' + (h^2 - k^2) Z = 0 \quad (39)$$

$$r^2 R'' + r R' + (k^2 r^2 - m^2) R = 0 \quad (40)$$

with solutions

$$\Theta_1(m\theta) = \cos(m\theta) \quad (41a)$$

$$\Theta_2(m\theta) = \sin(m\theta) \quad (41b)$$

$$Z_1(kz) = e^{-\alpha(k)z} \quad (42a)$$

$$Z_2(kz) = e^{\alpha(k)z} \quad (42b)$$

$$R_{m1}(kr) = J_m(kr) \quad (43a)$$

$$R_{m2}(kr) = N_m(kr) \quad (43b)$$

respectively. m is taken to be $0, 1, 2, \dots$ as the boundary conditions are periodic in θ . $J_m()$ and $N_m()$ are the Bessel- and Neumann functions of order m respectively. The Neumann function solution (43b) will be discarded as it has a singular point at the origin. This will be given further discussion under numerical integration.

The solution (37) becomes an angular expansion of the potential functions

$$\Phi(r, \theta, z) = \sum_{m=0}^{\infty} \Phi^m(r, z) \frac{\cos(m\theta)}{\sin(m\theta)} \quad (44)$$

$$\Lambda(r, \theta, z) = \sum_{m=0}^{\infty} \Lambda^m(r, z) \frac{\cos(m\theta)}{\sin(m\theta)} \quad (45)$$

$$\Psi(r, \theta, z) = \sum_{m=0}^{\infty} \Psi^m(r, z) \frac{\sin(m\theta)}{-\cos(m\theta)} \quad (46)$$

where

$$\Phi^m(r, z) = \int_0^{\infty} [a_1^m(k) e^{-z\alpha(k)} + a_2^m(k) e^{z\alpha(k)}] k J_m(rk) dk \quad (47)$$

$$\Lambda^m(r, z) = \int_0^{\infty} [b_1^m(k) e^{-z\beta(k)} + b_2^m(k) e^{z\beta(k)}] J_m(rk) dk \quad (48)$$

$$\Psi^m(r, z) = \int_0^{\infty} [c_1^m(k) e^{-z\beta(k)} + c_2^m(k) e^{z\beta(k)}] k J_m(rk) dk \quad (49)$$

$$\alpha(s) = \begin{cases} (k^2 - h^2)^{1/2}, & k^2 > \operatorname{Re}\{h^2\} \\ j(h^2 - k^2)^{1/2}, & k^2 < \operatorname{Re}\{h^2\} \end{cases} \quad (50)$$

$$\beta(s) = \begin{cases} (k^2 - g^2)^{1/2}, & k^2 > \operatorname{Re}\{g^2\} \\ j(g^2 - k^2)^{1/2}, & k^2 < \operatorname{Re}\{g^2\} \end{cases} \quad (51)$$

The displacement components u_z , u_r and u_θ are expanded according to

$$u_r(r, \theta, z) = \sum_{m=0}^{\infty} u_r^m(r, z) \frac{\cos(m\theta)}{\sin(m\theta)} \quad (52)$$

$$u_\theta(r, \theta, z) = \sum_{m=0}^{\infty} u_\theta^m(r, z) \frac{\sin(m\theta)}{-\cos(m\theta)} \quad (53)$$

$$u_z(r, \theta, z) = \sum_{m=0}^{\infty} u_z^m(r, z) \frac{\cos(m\theta)}{\sin(m\theta)} \quad (54)$$

If we derive the quantities u_r and u_θ by a direct application of the operator defined by (34), (35) on (44), (45) and (47), (48), we would, as we take into account

$$\frac{d}{dr} J_m(sr) = s J_{m-1}(sr) - \frac{m}{r} J_m(sr) \quad (55)$$

obtain results with different orders of the Bessel functions. It is, from a numerical point of view, desirable to have just one Bessel order in each equation.

If we form the linear combination of (34) and (35) with (52) and (53) as sum and difference, we get

$$\begin{aligned} u_r \pm u_\theta &= \\ \sum_{m=0}^{\infty} \left\{ u_r^m \frac{\cos(m\theta)}{\sin(m\theta)} \pm u_\theta^m \frac{\sin(m\theta)}{-\cos(m\theta)} \right\} &= \\ \left(\frac{\partial}{\partial r} \pm \frac{1}{r} \frac{\partial}{\partial \theta} \right) \Phi \pm \left(\frac{\partial}{\partial r} \mp \frac{1}{r} \frac{\partial}{\partial \theta} \right) \Psi + \frac{\partial}{\partial z} \left(\frac{\partial}{\partial r} \pm \frac{1}{r} \frac{\partial}{\partial \theta} \right) \Lambda \\ &= \sum_{m=0}^{\infty} \left\{ \left(\frac{\partial}{\partial r} \mp \frac{m}{r} \right) \Phi^m \frac{\sin(m\theta)}{-\cos(m\theta)} \right. \\ &\quad \left. \mp \left(\frac{\partial}{\partial r} \pm \frac{m}{r} \right) \Psi^m \frac{\cos(m\theta)}{\sin(m\theta)} \right. \\ &\quad \left. + \frac{\partial}{\partial z} \left(\frac{\partial}{\partial r} \mp \frac{m}{r} \right) \Lambda^m \frac{\sin(m\theta)}{-\cos(m\theta)} \right\} \end{aligned} \quad (56)$$

when we use the notation defined in (44) - (49).

We observe that the partial differentiation operation with respect to θ applied to the expressions for Φ , Ψ and Λ : (44) - (49), leads to a constant m (and of course alteration of the sine- and cosine-functions), so that the partial differentiation operator becomes equivalent to the operator defined by

$$\left(\frac{d}{dr} + \frac{m}{r}\right) J_m(sr) = s J_{m+1}(sr) \quad (57)$$

Hence, we have only one Bessel order for the positive- and negative-linear combinations respectively.

The trigonometric expansion given by (56) will of course be the same for all layers, differing only by the expansion coefficients. It is therefore sufficient to meet the boundary conditions in terms of the expansion coefficients

$$u_r^m(r, z) \pm u_\theta^m(r, z) = \left(\frac{\partial}{\partial r} + \frac{m}{r}\right) \Phi^m + \left(\frac{\partial}{\partial r} + \frac{m}{r}\right) \Psi^m + \frac{\partial}{\partial z} \left(\frac{\partial}{\partial r} + \frac{m}{r}\right) \Phi^m \quad (58)$$

which, when ((47)-(49)) is inserted becomes

$$\begin{aligned} u_r^m(r, z) \pm u_\theta^m(r, z) &= \int_0^\infty [a_1^m(s) s e^{-z\alpha(s)} \pm a_2^m(s) s e^{z\alpha(s)} \\ &\pm b_1^m(s) \beta(s) e^{-z\beta(s)} \pm b_2^m(s) \beta(s) e^{z\beta(s)} \\ &+ c_1^m(s) s e^{-z\beta(s)} + c_2^m(s) s e^{z\beta(s)}] s J_{m+1}(rs) ds \end{aligned} \quad (59)$$

The corresponding development of u_z comes considerably easier as we observe that the part of the differential operator (36) which operates on Λ is $\nabla^2 - (\partial/\partial z)^2$, which by (25C) becomes

$$\nabla^2 - \frac{\partial^2}{\partial z^2} \Lambda = -(g^2 + \frac{\partial^2}{\partial z^2}) \Lambda \quad (60)$$

so that we can write

$$u_z^m(r, z) = \int_0^\infty [-a_1^m(s) \alpha(s) e^{-z\alpha(s)} + a_2^m(s) \alpha(s) e^{z\alpha(s)} + b_1^m(s) s e^{-z\beta(s)} + b_2^m(s) s e^{z\beta(s)}] s J_m(rs) ds \quad (61)$$

The following boundary conditions at the horizontal interfaces involve the stress components T_{zz} , T_{rz} and $T_{\theta z}$. If these are expanded like (44), (45) and (46) respectively, use of Hooke's law leads to the following expressions for the expansion coefficients

$$\begin{aligned} T_{zz}^m(r, z) &= \lambda \nabla^2 u_z^m(r, z) + 2\mu \frac{\partial}{\partial z} u_z^m(r, z) \\ &= \mu \int_0^\infty [a_1^m(k) (2k^2 - g^2) e^{-z\alpha(k)} + (2k^2 - g^2) a_2^m(k) e^{z\alpha(k)} - b_1^m(k) 2k\beta(k) e^{-z\beta(k)} + b_2^m(k) 2k\beta(k) e^{z\beta(k)}] k J_m(rk) dk \quad (62) \end{aligned}$$

$$\begin{aligned} T_{rz}^m(r, z) \pm T_{\theta z}^m(r, z) &= \\ \mu \left(\frac{\partial}{\partial z} (u_r^m(r, z) \pm u_\theta^m(r, z)) + \left(\frac{\partial}{\partial r} \pm \frac{m}{r} \right) w_z^m(r, z) \right) \\ &= \mu \int_0^\infty [-a_1^m(k) 2k\alpha(k) e^{-z\alpha(k)} \pm a_2^m(k) 2k\alpha(k) e^{z\alpha(k)} + b_1^m(k) (2k^2 - g^2) e^{-z\beta(k)} \pm b_2^m(k) (2k^2 - g^2) e^{z\beta(k)} - c_1^m(k) k\beta(k) e^{-z\beta(k)} + c_2^m(k) k\beta(k) e^{z\beta(k)}] k J_{m+1}(kr) dk \quad (63) \end{aligned}$$

It should be noted that the use of the linear combinations (59) and (63) in the boundary conditions rather than the components has the effect that all coefficients relating to the unknown arbitrary functions (a_1, a_2, b_1, b_2, c_1 and c_2) will be independent of the Fourier order m . This is obviously very important for the efficiency of the numerical solution.

For fluid layers only the potential $\phi(r, \theta, z)$ will be present, and the expansion coefficients for the displacements are obtained directly

from (51) and (59) by setting b_1^m, b_2^m, c_1^m and c_2^m to zero. The shear stresses vanish identically, whereas (62) has to be replaced by

$$\begin{aligned} \tau_{zz}^m(r, z) &= \lambda \nabla^2 \phi^m(r, z) \\ &= -\lambda h^2 \int_0^\infty [a_1^m(k) e^{-z\alpha(k)} + a_2^m(k) e^{z\alpha(k)}] k J_m(rk) dk \end{aligned} \quad (64)$$

2.4 Source field

A simple compressional source placed at the point $\{r_1, \theta_1, z_1\}$ will produce the following field in an infinite homogeneous medium, [9]

$$\tilde{\phi}_1(r, \theta, z) =$$

$$\frac{S_1}{4\pi w} \sum_{m=0}^{\infty} \epsilon_m \cos m(\theta - \theta_1) \int_0^{\infty} J_m(r_1 k) \frac{e^{-\alpha(k)|z-z_1|}}{\alpha(k)} k J_m(rk) dk \quad (65)$$

where S_1 is the source strength, which is generally complex to account for the actual phase of the source. The factor ϵ_m , due to the expansion of the exponential function in a Neumann series [9], is

$$\epsilon_m = \begin{cases} 1, & m = 0 \\ 2, & m > 0 \end{cases} \quad (66)$$

If more than one source is present within a layer, the contributions are simply added to yield

$$\tilde{\phi}(r, \theta, z) =$$

$$\frac{1}{4\pi w} \sum_{m=0}^{\infty} \epsilon_m \int_0^{\infty} \left[\sum_{i=1}^N S_i \cos m(\theta - \theta_i) J_m(r_i k) \right] \frac{e^{-\alpha(k)|z-z_1|}}{\alpha(k)} k J_m(rk) dk \quad (67)$$

where N is the number of sources. The potential $\tilde{\phi}(r, \theta, z)$ is now expanded like (44) and the coefficients are easily obtained as

$$\tilde{\phi}^m(r, \theta, z) =$$

$$\frac{\epsilon_m}{4\pi w} \int_0^{\infty} \left[\sum_{i=1}^N S_i \begin{cases} \cos m\theta_i \\ \sin m\theta_i \end{cases} J_m(r_i k) \right] \frac{e^{-\alpha(k)|z-z_1|}}{\alpha(k)} k J_m(rk) dk \quad (68)$$

The expansion coefficients for the Cartesian displacements components follow from ((52), (53) and (54))

$$\begin{aligned} \tilde{u}_z^m(r, z) &= \\ &= \frac{\epsilon_m}{4\pi\omega} \int_0^\infty \sum_{i=1}^N \frac{\cos(m\theta_i)}{\sin(m\theta_i)} \operatorname{sign}(z-z_i) J_m(r_1 k) \frac{e^{-\alpha(k)|z-z_i|}}{\alpha(k)} k J_m(rk) dk \end{aligned} \quad (69)$$

$$\begin{aligned} \tilde{u}_r^m(r, z) \pm \tilde{u}_\theta^m(r, z) &= \\ &= \frac{\epsilon_m}{4\pi\omega} \int_0^\infty \sum_{i=1}^N \frac{\cos(m\theta_i)}{\sin(m\theta_i)} J_m(kr_1) \frac{e^{-\alpha(k)|z-z_i|}}{\alpha(k)} k J_{m\pm 1}(rk) dk \end{aligned} \quad (70)$$

and use of Hooke's law yield the following expansion coefficients for the stresses involved in the boundary conditions

$$\begin{aligned} \tilde{T}_{zz}^m(r, z) &= \\ &= \frac{\mu\epsilon_m}{4\pi\omega} \int_0^\infty [(2k^2 - g^2) \sum_{i=1}^N \frac{\cos(m\theta_i)}{\sin(m\theta_i)} J_m(kr_1) \frac{e^{-\alpha(k)|z-z_i|}}{\alpha(k)} k J_m(rk) dk \end{aligned} \quad (71)$$

$$\begin{aligned} \tilde{T}_{rz}^m(r, z) \pm \tilde{T}_{\theta z}^m(r, z) &= \\ &= \frac{\mu\epsilon_m}{4\pi\omega} \int_0^\infty [2k \sum_{i=1}^N \frac{\cos(m\theta_i)}{\sin(m\theta_i)} \operatorname{sign}(z-z_i) J_m(kr_1) e^{-\alpha(k)|z-z_i|} k J_{m\pm 1}(kr) dk \end{aligned} \quad (72)$$

In the case of a fluid layer eq. (71) must be modified to

$$\begin{aligned} \tilde{T}_{zz}^m(r, z) &= \\ &= \frac{\lambda h^2 \epsilon_m}{4\pi\omega} \int_0^\infty \sum_{i=1}^N \frac{\cos(m\theta_i)}{\sin(m\theta_i)} J_m(kr_1) \frac{e^{-\alpha(k)|z-z_i|}}{\alpha(k)} k J_m(kr) dk \end{aligned} \quad (73)$$

Here only simple compressional sources have been considered, but shear wave sources, involving the potential Λ or Ψ , can be treated in exactly the same way, leading to integral representations similar to eqs (69) - (72) for the field parameters.

2.5 Solution technique

2.5.1 Numerical integration of the Bessel transform

The integrals of ((47)), (48) and (49) may be written in a simplified manner as

$$\int_0^{\infty} G(k) J_n(kr) dk \quad (74)$$

The Bessel function may be written as the sum

$$2 J_n(z) = H_n^{(1)}(z) + H_n^{(2)}(z) \quad (75)$$

where $H_n^{(1)}()$ and $H_n^{(2)}()$ represent the Hankel functions of first and second kind, order n respectively. For the time-dependent solution chosen here ($\exp(j\omega t)$), the Hankel functions of first and second kind represent in- and outgoing waves respectively. As there are no backscatter elements included in the model, the Bessel function may be approximated by the Hankel function of the second kind. This approximation is of course not valid in the region between source(s) and the center axis. Otherwise the validity of this approximation is discussed in [5]. The Hankel function is substituted for its large argument approximation as given by

$$H_n^{(2)}(z) \approx \left(\frac{2}{\pi z} \right)^{1/2} e^{-j(z - \frac{\sqrt{\pi}}{2} - \frac{\pi}{4})} \quad (76)$$

We will evaluate the integral at discrete steps according to

$$k = k_0 + n\Delta k \quad n = 0, 1, 2, \dots, N-1 \quad (77a)$$

$$r = r_0 + m\Delta r \quad m = 0, 1, 2, \dots, N-1 \quad (77b)$$

$$\Delta k \Delta r = 2\pi/N \quad (77c)$$

Insertion of (76) and (77) into (74), and substituting order of integration and summation yields

$$\frac{1}{2} \left(\frac{2}{\pi r} \right)^{1/2} \Delta k e^{-j(k_0 r - \frac{\pi}{4} - \frac{v\pi}{2})}$$

$$\sum_{n=0}^{N-1} G(k_0 + n\Delta k) \frac{e^{-jn\Delta k r_0}}{(k_0 + n\Delta k)^{1/2}} e^{-j(\frac{2\pi}{N} nm)} \quad (78)$$

This expression is clearly a preweighting of the integrand and thereafter a discrete Fourier transform. It is evaluated by means of the FFT algorithm, and thereafter postweighting.

2.5.2 The global matrix method

Solution of the problem at hand implies finding the values of the potentials a, b and c that satisfy the pertinent source and boundary conditions.

At each interface u_z and T_{zz} must be continuous. At solid/solid interfaces we must in addition require that u_r, u_θ, T_{rz} and $T_{\theta z}$ be continuous. At solid/liquid interfaces the shear stresses must vanish. We express these boundary conditions with (34), (35), (36) and the expressions for stresses obtained by the use of Hookes law. These boundary conditions may readily be reformulated in terms of the angular expansion coefficients which, when collected in a column vector become:

$$F^m(r, z) = \begin{bmatrix} u_z^m(r, z) \\ u_r^m(r, z) + u_\theta^m(r, z) \\ u_r^m(r, z) - u_\theta^m(r, z) \\ T_{zz}^m(r, z) \\ T_{rz}^m(r, z) + T_{\theta z}^m(r, z) \\ T_{rz}^m(r, z) - T_{\theta z}^m(r, z) \end{bmatrix} \quad (79)$$

The unknown potentials are so defined that the depth coordinate z within this layer is 0 at the upper layer interface. The boundary conditions at interface n which is the lower interface of layer n may thus be stated:

$$F_n^m(r, z_n) + \tilde{F}_n^m(r, z_n) - F_{n+1}^m(r, 0) - \tilde{F}_{n+1}^m(r, 0) = 0 \quad (80)$$

where subscript n denotes the layer number, z_n denotes the thickness of layer n and the terms with tilde \sim as before denotes source terms. Insertion of (61), (59), (62) ((64) in the fluid case) and (63), interchanging order of integration and summation, reduces (80) to a set of integrands which must vanish. Thus we are left with a set of linear equations in the unknown potential functions and the source contributions which becomes

$$A_{n,1} B_n^m - A_{n+1,u} B_{n+1}^m = R_{n+1,u}^m - R_{n,1}^m \quad (81)$$

where the unknown potential functions for layer n are

$$B_n^m(k) = \begin{bmatrix} a_{1,n}^m(k) \\ b_{1,n}^m(k) \\ c_{1,n}^m(k) \\ a_{2,n}^m(k) \\ b_{2,n}^m(k) \\ c_{2,n}^m(k) \end{bmatrix} \quad (82)$$

For a solid layer the matrix A for the upper interface in layer n is

$$A_{n,u}(k) = \begin{bmatrix} -\alpha & k & 0 & \alpha & k & 0 \\ -k & \beta & k & -k & -\beta & k \\ k & -\beta & k & k & \beta & k \\ (2k^2 - g^2)\mu & -2k\beta\mu & 0 & (2k^2 - g^2)\mu & 2k\beta\mu & 0 \\ 2k\alpha\mu & -(2k^2 - g^2)\mu & -k\beta\mu & -2k\alpha\mu & -(2k^2 - g^2)\mu & k\beta\mu \\ -2k\alpha\mu & (2k^2 - g^2)\mu & -k\beta\mu & 2k\alpha\mu & -(2k^2 - g^2)\mu & k\beta\mu \end{bmatrix} \quad (83)$$

while for a liquid layer, the matrix becomes

$$A_{n,u}(k) = \begin{bmatrix} -\alpha & 0 & 0 & \alpha & 0 & 0 \\ -k & 0 & 0 & -k & 0 & 0 \\ k & 0 & 0 & k & 0 & 0 \\ -\lambda h^2 & 0 & 0 & -\lambda h^2 & 0 & 0 \\ 0 & 0 & 0 & 0 & 0 & 0 \\ 0 & 0 & 0 & 0 & 0 & 0 \end{bmatrix} \quad (84)$$

The matrix for the lower interface of a layer is obtained by multiplying each element with the appropriate exponential as given by (61) - (64) with $z=z_n$ i.e:

$$A_{n,l}(k) = A_{n,u}(k) I_n(k) \quad (85)$$

where

$$I_n(k) = \begin{bmatrix} e^{-\alpha(k)z_n} & 0 & 0 & 0 & 0 & 0 \\ 0 & e^{-\beta(k)z_n} & 0 & 0 & 0 & 0 \\ 0 & 0 & e^{-\beta(k)z_n} & 0 & 0 & 0 \\ 0 & 0 & 0 & e^{\alpha(k)z_n} & 0 & 0 \\ 0 & 0 & 0 & 0 & e^{\beta(k)z_n} & 0 \\ 0 & 0 & 0 & 0 & 0 & e^{\beta(k)z_n} \end{bmatrix} \quad (86)$$

The source contribution vector is

$$R_n^m = \frac{\epsilon_m}{4\pi\omega} \sum_{l=1}^N \frac{\cos(m\theta_l)}{\sin(m\theta_l)} J_m(kr_l) e^{-\alpha|z-z_l|} \begin{bmatrix} -\operatorname{sgn}(z-z_l) \\ -k/\alpha \\ k/\alpha \\ \mu(2k^2 - g^2)/\alpha \\ 2k\mu\operatorname{sgn}(z-z_l) \\ -2k\mu\operatorname{sgn}(z-z_l) \end{bmatrix} \quad (87)$$

where $z=0$ and z_n for upper and lower boundaries respectively.

Finally the local sets of boundary equations are mapped into a global set of equations

$$\begin{bmatrix} [A_{1,1}] [-A_{2,u}] & & & \\ & [A_{2,1}] [-A_{3,u}] & & \\ & & [A_{3,1}] [-A_{4,u}] & \\ & & & \ddots \\ & & & & [A_{N-1,1}] [-A_{N,u}] \end{bmatrix} \begin{bmatrix} B_1^m \\ B_2^m \\ \vdots \\ \vdots \\ B_N^m \end{bmatrix} =$$

$$\begin{bmatrix} R_{2,u}^m \\ R_{3,u}^m \\ R_{4,u}^m \\ \vdots \\ R_{N,u}^m \end{bmatrix} = \begin{bmatrix} R_{1,1}^m \\ R_{2,1}^m \\ R_{3,1}^m \\ \vdots \\ R_{N-1,1}^m \end{bmatrix}$$

(88)

The global matrix method, as opposed to matrizant methods[3] is presented in [9].

2.5.3 Numerical considerations

A commonly known problem with the matrizant method on which FFP models have been based[3], is encountered when dealing with thick layers in the evanescent region of the horizontal wavenumber spectrum. The wave amplitudes, represented by depth dependent exponential functions with positive real arguments, may attain large values. It is of course obvious from physical considerations, that the energy content cannot grow beyond finite values, so this situation must be considered as a numerical artifact. Several techniques are utilized to remedy this situation.

The matrices $A_{n,l}$ and $A_{n,u}$ are made dimensionless by dividing the stress- and pressure-related coefficients by $\omega^2 \varrho_n$ and by the horizontal wavenumber respectively. ϱ_n denotes the density of an intermediate layer. This will ensure that the coefficients are within the same order of magnitude.

Each layer is described in a separate local coordinate system with origin at its upper surface. This will ensure that the value of the depth does not exceed the layer thickness.

The order of potentials, as defined by (82) ensures that the coefficients, which attain high values due to the above mentioned exponential functions, come close to the diagonal of the global matrix.

These remedies will, together with standard pivoting by columns, ensure that the solution of (88) by means of Gaussian elimination, will be unconditionally stable[7].

The above statement must, however, be slightly modified when we have a source in a thick layer with evanescent propagation conditions. Numerical instability due to the nonvanishing pertinent row of the righthand side of (88), may occur. This problem is easily circumvented by introducing dummy-interfaces just above and below the source(s).

Coherent sources on both sides of a thick layer may also represent a numerical problem, but as this situation is regarded as being less important in most physical applications, it is not considered a serious limitation. It is of course possible to solve the problem separately for both these sources and superpose the solutions.

2.6 Numerical example: a point source in free space

The example of a point source in free space is a well suited example for verification of the model as the correct result is readily calculated as $20\log(r)$. Free space means a water layer, containing source and receiver, surrounded by upper- and lower-halfspaces consisting of water with identical parameters.

This example is, however, rather a challenge for the FFP model, as the integrand easily becomes undersampled due to the branchpoint arising from the square root in the denominator of (73) (the reader is also referred to (50)). Here, the integrand is sampled at 8196 points ranging from $628 \times 10^{-6} \text{ m}^{-1}$ to 0.465 m^{-1} .

Figure 2.1 shows a comparison between model outputs with the source located on the center axis and also with the source displaced 100 m in positive x-direction from the center axis, i.e. the model is run in two- and three-dimensional modes respectively. In both cases the frequency is 100 Hz, the receiver is located 40 m above the source. The three-dimensional case required an angular expansion order of 110. Curves a and b show the transmission loss for the two-dimensional- and three-dimensional-cases respectively. The region of validity for the computed solution begins at a greater distance from the source in the three-dimensional case, as the approximation to the higher order Hankel functions has larger remainders than what is the case for the 0-order approximation. The computed solution is of course not valid between the source and center axis as only the Hankel-function corresponding to outward propagating waves is included. Figure 2.2 shows the computed transmission loss in all directions for the three-dimensional example. The line markers $x=0$ and $y=0$ are drawn.

3 THE INVERSE PROBLEM

3.1 Introduction

The objective for solving the inverse problem is to determine the parameters which have significant influence on sound propagation in the water layer(s) in a shallow water environment. Determining the parameters within "acceptable" confidence bounds, will enable us to model their effects and thereby predict sound propagation in the water layer under the influence of the ocean bottom.

To my knowledge, there has not been any earlier reports of attempts to infer ocean bottom parameters based on the methods to be utilized here.

There is no commonly accepted definition making a clear and concise distinction between deep and shallow water. The term "shallow water" is used here to imply an acoustic environment and an acoustic wavelength sufficiently large (with respect to depth) that sound propagation is suited for modelling by wave theory.

While sound propagation in deep water is well handled by ray theory, multiple reflections in the shallow water situation create a rather complicated ray picture. If we, as here, limit ourselves to a horizontally stratified medium, multiple bounces may interfere constructively or destructively, and thus show a resonator effect. This effect is, as will be demonstrated, readily described in the frequency-horizontal wavenumber (F-K) domain. A projection of the signal space occurring in a horizontally layered medium into the F-K domain will readily show modes of propagation, their phase- and group velocities, cut off frequencies and also important features of the ocean bottom.

The term "mode" is used in a more free sense than in most of the other literature. Here it is taken to mean the loci of points in the F-K domain where constructive interference occurs, not limited to the discrete region of the K-spectrum. The term "normal modes" (normal =

orthogonal) does not enter into this discussion as we do not define an appropriate inner product onto the observation space. Elements of such an inner product space would be values as a function of depth.

The nomenclature for characterization of interface waves is adopted from [18]. A Rayleigh wave can occur on the interface between a solid and vacuum, a Scholte wave between a solid and a liquid and a Stoneley wave on the interface between two solids.

A suitable observation space for projection into the F-K space is a horizontal array. In this work, data from a seismic research vessel towing a super long air gun array (SLAG) and a 52-element hydrophone array is used, not because this particular configuration is ideal for our purpose, but because it is available.

3.2 Some basic properties of a monolayer waveguide

It is not intended that this chapter shall be an exhaustive development of waveguide theory. The purpose is just to establish some fundamental properties which will aid us in understanding how to interpret an F-K diagram. The complete theory is, of course, covered implicitly in the previous section on the forward problem.

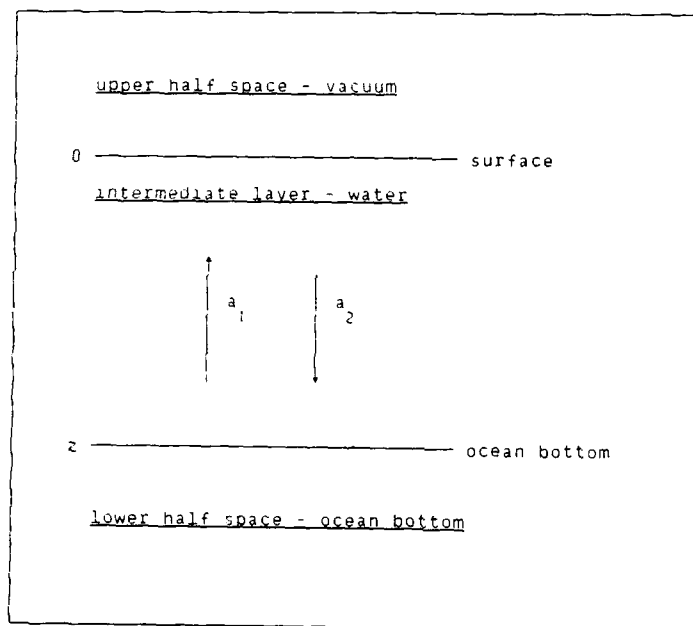


Figure 3.1 A monolayer waveguide. a_1 and a_2 refer to equation (54)

The essential elements of a water layer bounded by surface and ocean bottom are shown in figure 3.1. Referring to equation (64), the depth dependent part of the separable solution consists of an up- and downward propagating component. The boundary conditions are equivalent with reflections occurring at the boundaries. Constructive interference between a_1 and a_2 will occur when

$$R_s(\varphi) e^{j\theta_s(\varphi)} R_b(\varphi) e^{j\theta_b(\varphi)} e^{-j2\alpha(\omega, k)z} = 1 \quad (89)$$

where $R(\varphi) e^{j\theta(\varphi)}$ are plane wave reflection coefficients and φ is a characteristic angle, either incident or grazing. The subscripts s and b refer to surface and bottom respectively. (89) is equivalent to

$$R_s R_b = 1 \quad (90a)$$

and

$$\theta_s + \theta_b + 2\alpha z = (1-n)2\pi, \quad n = 0, 1, 2, 3, \dots \quad (90b)$$

(90a) implies a lossless medium and totally reflecting boundaries, corresponding to a resonator with an infinite Q -factor. This is of course an approximation. We will not dwell upon its validity, as the purpose for its application is to establish a phenomenological framework for a basic understanding of waveguide properties. (90b) is a resonance condition. As an approximation, we will assume the reflection coefficient at the surface to be -1 for all φ . The reflection coefficient, as well as the impedance, for the ocean bottom represent a necessary and sufficient description of the influence of the ocean bottom properties on sound propagation in the water layer for a horizontally stratified medium. The effect of more than one ocean bottom layer may be collected in the ocean bottom reflection coefficient, but it then becomes a function of both frequency and horizontal wavenumber as reflections are related to incidence angle and propagation between boundaries is related to vertical wavenumber.

3.3 A test case

Figure 3.3 shows an F-K diagram of a test case with parameters as shown in figure 3.2. The source is 7.5 m- and the receiver is 14 m below the ocean surface. The diagram is the module of the preweighted integrand given by (78). Radiating from the origin are five line markers which in descending order of phase velocity (ω/k) indicate the loci of points constituting constant:

- compressional wave phase velocity in the ocean bottom
- shear wave phase velocity in the ocean bottom
- Rayleigh wave velocity at the ocean bottom interface
- compressional wave phase velocity in the water layer
- Scholte wave velocity at the water/solid interface

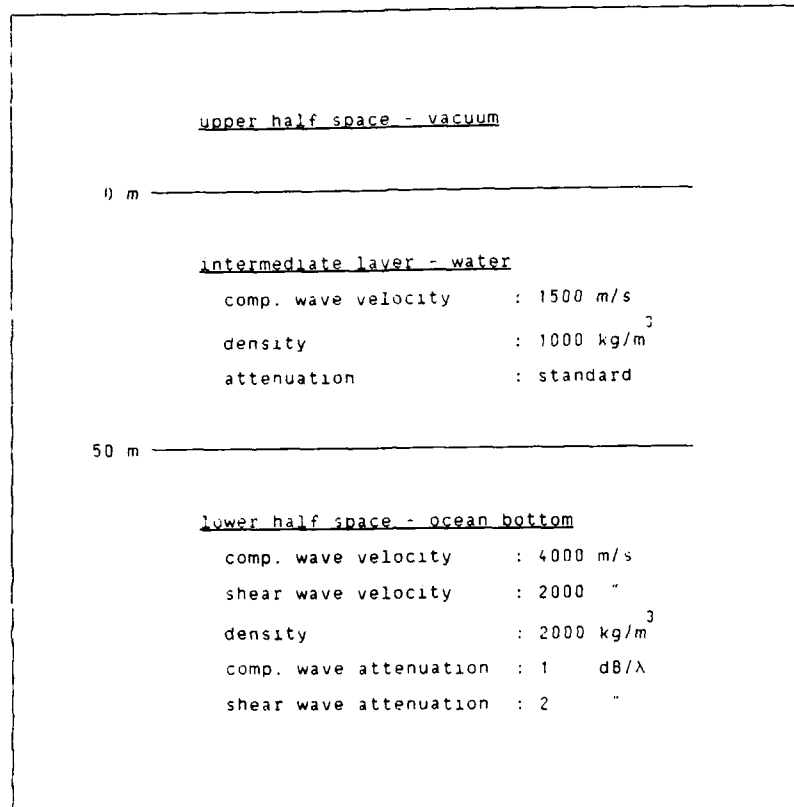


Figure 3.2 Environmental parameters for single bottom layer test case

On the ordinate axis $k \geq 0$. In the order of increasing frequency, the 0., 1., 2., 3. and just barely the 4. mode may be identified. The 0. mode originates at the origin.

Figure 3.4 shows module and phase of both reflection coefficient and ocean bottom impedance for the same test case. The left column from top to bottom shows module of reflection coefficient including the evanescent region, module of reflection coefficient excluding the evanescent region and finally the phase of the reflection coefficient including the evanescent region. The right column shows module and phase of ocean bottom impedance, both including the evanescent region. For abscissa the horizontal phase velocity is chosen as it offers an

easy comparison with the characteristic velocities of the environment. The horizontal phase velocity relates to various alternative parameters as

$$v_h = \frac{\omega}{k} = \frac{c_c}{\sin(\varphi_1)} = \frac{c_c}{\cos(\varphi_g)} = \frac{1}{p} \quad (91)$$

where φ_1 and φ_g are incident- and grazing angles respectively and p is slowness.

Figures 3.5 to 3.10 are identical to figure 3.4, except for the broken lines which indicate perturbation of environmental parameters. In order of appearance, the effects of the following parameter variations are shown:

- compressional wave phase velocity in the water layer
- compressional wave phase velocity in the ocean bottom
- shear wave phase velocity in the ocean bottom
- density in the ocean bottom
- compressional wave attenuation in the ocean bottom
- shear wave attenuation in the ocean bottom

The source and receiver are located fairly close to the ocean surface. As we are dealing with a homogeneous water layer, there is no inherent mechanism for trapping acoustic energy in a channel close to the surface, hence energy produced by the source and detected by our receiver will be influenced by bottom properties and constructive interference as indicated by (89).

The 0. and the higher order modes will be commented on separately, as their behaviour differs.

3.3.1 The 0. mode

The 0. mode originates at the origin, it has no pronounced low frequency cut-off. At the origin, where ω and s approach zero, the vertical wavenumber ((50).(26)) approaches zero. As the depth is constant, αz in (90b) may be taken to be zero, thus, for $n=0$, the phase of the bottom reflection coefficient approaches π .

As is well known, the Rayleigh wave occurs at the interface between a solid and vacuum. In the solid, it is evanescent in the z -direction and is thus a surface wave with horizontal wave velocity below the free shear wave velocity of the solid. For a liquid/solid interface, the Rayleigh wave becomes a pseudo-Rayleigh wave: its horizontal phase velocity becomes complex. For a vacuum/solid interface, a Rayleigh wave implies vertical displacement and vanishing normal stress at the solid/vacuum interface: vanishing impedance. The curve for module of ocean bottom impedance in figure 3.4 shows a dip at what is here the pseudo-Rayleigh wave horizontal phase velocity: 1865.6 m/s.

From the graph of the ocean bottom reflection coefficient in figure 3.4, it can be seen that while the module has a dip at the Rayleigh velocity, the phase equals $-\pi$. Solution of (90b) for $n=0$ requires that the vertical wavenumber is equal to zero. Returning to figure 3.3, we can see that as the 0. mode develops from the origin, at a phase velocity asymptotically equal to the Rayleigh wave velocity (actually figure 3.3 does not show this accurately, but a detail of this corner near the origin would), its energy content increases due to increasing module of reflection coefficient. For increasing frequency, figure 3.3 shows the phase velocity to decrease and go below the water velocity and approach the Scholte wave velocity. From figure 3.4: as the horizontal phase velocity decreases from the Rayleigh value, the module increases and the phase increases through a peak and returns to $-\pi$ at the water wave velocity. Again, we have a solution where the vertical wavenumber α is zero, but now because the horizontal wavenumber equals the wavenumber of a free plane wave in water. In further decreasing the horizontal phase velocity, we come into the evanescent region, characterized by a real (pure real for a lossless medium) vertical wavenumber. As we enter into the evanescent region, the acoustic coupling between surface and bottom diminishes, and the 0. mode fades out. Obviously, if properly excited, the 0. mode will transfer energy into a pure Scholte surface wave. The Scholte wave velocity is for this case 1399.2 m/s. Figure 3.4 shows a strong peak in module of reflection coefficient at the Scholte wave velocity.

Now having given an outline of the basic mechanisms of the 0. mode, we can use the perturbed reflection coefficients of figures 3.5 to 3.10 to look into how variation of the environmental parameters manifest themselves.

As is well known, the Rayleigh velocity is governed by properties of the solid, while the Scholte root is governed by water properties as well. For more details, the reader is referred to appendix 1 and also to [18].

The location of the dip in module of reflection coefficient at the Rayleigh wave velocity is highly dependent upon the shear wave velocity, figure 3.7, and barely upon compressional wave velocity, density and shear wave attenuation. The dip value, however, is strongly dependent upon the shear wave velocity and attenuation.

3.3.2 The higher order modes

The higher order modes ($n=1,2,\dots$ in (90b)) have the same general behaviour and will therefore be commented upon collectively. It is found advantageous to divide the higher order modes into separate regions characterized by the horizontal phase velocities as follows:

- continuous region: $c_c < v_h < \infty$
- intermediate region: $c_s < v_h < c_c$
- discrete region: $c_w < v_h < c_s$

As mentioned earlier in this chapter, the F-K plot in figure 3.3 is separated into these regions by the line markers.

The continuous region. For the continuous region, we note that, contrary to the 0. mode, the higher order modes have a low frequency cutoff. This is clearly seen in figure 3.3 where the modes originate from the axis $s=0$. For $s=0$, the vertical wavenumber α becomes w/c . From figure 3.4 and figures 3.5 to 3.10, it is seen that for this region the phase of the reflection coefficient equals zero for all parameter variations. Consequently, (90b) simplifies to

$$\frac{w}{c} z = \frac{\pi}{2} (2n-1) \quad , \quad n=1,2,3,\dots \quad (92)$$

As the horizontal phase velocity is greater than the compressional (and of course the shear) velocity of the ocean bottom, energy is leaked into the bottom as both compressional- and shear waves, and we do not have a trapped wave in the water layer. Consequently, the transmission loss is so high in this region that it is usually considered as non propagating. It should be noted, however, that for this test case, we are considering a hard ocean bottom with significant impedance contrast between water and bottom. Hence, even for the continuous region, the reflection coefficient is appreciably high.

While, as a function of increasing horizontal wavenumber, the horizontal phase velocity decreases from infinity, the group velocity (dw/ds) increases from zero. For this region, the increase in group velocity is caused solely by variations in frequency and horizontal wavenumber such that the vertical wavenumber α remains constant.

For the continuous region, the module of reflection coefficient is dependent on the impedance contrast between water and solid, hence the phase velocities and density. As the phase remains unchanged, these parameters do not influence the loci of maxima in the F-K domain.

Horizontal phase velocity equal to ocean bottom compressional velocity.

The highest velocity line marker in figure 3.3, indicating a horizontal phase velocity of 4000 m/s equal to the compressional wave velocity of the ocean bottom, passes through peaks: one for each of the higher order modes. These peaks are clearly seen as a peak in module of reflection coefficient in figure 3.4. Figure 3.6 shows how

the peak "follows" ocean bottom compressional wave velocity. Figure 3.7 shows how its shape is influenced by ocean bottom shear velocity. It should also be noted that the peak is slightly influenced by ocean bottom compressional wave attenuation, unaffected by ocean bottom shear wave attenuation and also that it is approximately at this point the phase of the reflection coefficient begins to differ from zero.

Intermediate region.

In the intermediate region, free propagating shear waves may be coupled into the ocean bottom, while compressional waves undergo total reflection. The group velocity increases significantly in this region.

Horizontal phase velocity equal to ocean bottom shear velocity.

When the horizontal phase velocity equals the ocean bottom shear velocity, the bottom becomes totally reflecting. Hence neither compressional- nor shear waves are coupled into the ocean bottom as free propagating waves. According to [1], the group velocity equals the phase velocity: the ocean bottom shear wave velocity.

The discrete region.

The discrete region, so termed because the horizontal wavenumber spectrum for a given frequency becomes discrete and contains the propagating part of the energy. As neither shear- nor compressional waves are transmitted into the ocean bottom half space, all energy is trapped in the water layer: we have a wave guide effect. In this region, the phase velocity converges from above- and the group velocity converges from below to the phase velocity of the water layer.

3.4 Description of data collection and system response

The measured data have kindly been supplied by the Norwegian Petroleum Directorate. They were gathered by the seismic vessel M/V Malene Østervold operated by GECO. The source was an airgun array and the receiver was a seismic streamer, both towed behind the vessel.

The data were collected on 31 July 1979, north of Bear Island: $75^{\circ}20'N$ $18^{\circ}50'E$. This area is characterized by its hard bottom, thus giving rise to multiple reflections between ocean-surface and -bottom.

The data are identified as line 7520-79 shots nr. 9191 to 9296.

The streamer is towed at 14 m water depth. It consists of 52 hydrophone groups, the distance between their centerpoints are 50 m. A group is formed of two subgroups each of length 22 m and consisting of 32 equispaced hydrophones. The spacing between subgroups is 3 m. The signals from each hydrophone within a group are summed without weighting.

The hydrophone group separation, 50 m, implies a spatial angular sampling rate (wavenumber) of 0.126 m^{-1} and a Nyquist rate of 0.063 m^{-1} .

When taking the effects of the ocean surface into account as the Lloyd-mirror effect, the modulus of a horizontal wavenumber response becomes

$$H_{st} = \left| \frac{1 - e^{-jN\gamma}}{1 - e^{-j\gamma}} (1 + e^{js\Delta}) (1 + e^{-j2\Gamma_1}) \right| \quad (93)$$

where

$$\gamma = s\delta \quad (94)$$

$$\Gamma_1 = \left(\left(\frac{u}{c} \right)^2 - s^2 \right)^{1/2} d_1 \quad (95)$$

and δ is the hydrofon spacing (22/31 m), Δ is the distance between the first hydrophones in a subgroup (25m), N is the number of hydrophones

within a subgroup (32) and d_1 is the nominal streamer depth (14m).

The signals from each group are sampled successively at a rate of 250 Hz. There has not been performed any filtering in the low frequency end of the signal spectrum, the high frequency end has been filtered through a low-pass filter 3 dB down at 64 Hz decaying 72 dB/octave.

The distance from the source centerpoint to the middle of the first hydrofon (offset) is 180.75 m.

The source has been towed at a nominal depth of 7.5 m. The airgun array was fired every 50 m. The frequency spectrum for the source is shown in figure 3.12. If we assume the source geometry depicted in figure 3.11 and include the Lloyd-mirror effect, we obtain the modulus of the source horizontal wavenumber spectrum as

$$H_{s0} = \left| (1 + e^{-j2\Gamma_2}) \sum_{i=1}^5 e^{j\delta_i s} \right| \quad (96)$$

where

$$\Gamma_2 = ((\frac{\omega}{c})^2 - s^2)^{1/2} d_2 \quad (97)$$

δ_1 denotes the distance from first to i-th. source and d_2 the source depth. The effects of source spacing transversal to centerline of ship's track have been disregarded.

Multiplication of (93) and (96) gives an estimate of the modulus of the horizontal wavenumber respons of the data collection system. This, together with a piecewise linear approximation of the source frequency spectrum, is shown in figure 3.13. The response is normalized with respect to total power. Figure 3.13 a shows a surface plot on a linear scale, while figure 3.13 b shows the same data in a contour plot on a logarithmic scale with 5 dB between contours. Lloyd-mirror effect of source and streamer appear as a null radiating from the origin to {0.12, 28} while the null originating in {0.51} is caused by the streamer. The corresponding null produced by the source falls outside the figure bounds. The source sidelobes are seen as maxima and minima at constant k-values. The streamer produces a first minimum at a horizontal wavenumber of approximately 0.12 m^{-1} and therefor acts as a spatial low pass filter with first minimum at twice the Nyquist frequency.

3.5 Preprocessing and display of measured data

In order to bring the measured data on a form comparable to the model output, inverse weighting corresponding to the post-FFT weighting given in (78) is performed. It has been experienced that it is an advantage to Hanning weight the data in the X-direction.

A two-dimensional FFT is performed. The FFT lengths are 64 points in X-direction and 1024 points in T-direction.

The displayed data is limited to 60 points in K-direction and 250 points in F-direction. It is common within the seismic community to display the K-direction showing both positive- and negative values of horizontal wavenumber, but as we have good signal to noise ratio, it is fair to assume that energy propagation in positive direction (from source and aft along array) is dominant. This agrees well with the analyzed data. We have therefore displayed the first 60 points in K-direction in the order of increasing FFT-bin. The frequency direction is limited to 250 points as we do not have significant energy content above this frequency.

A normalization based on a total power content in the displayed data to be equal to unity is performed. The amplitude of the F-K spectrum is displayed on a linear scaled surface plot and a logarithmic contour plot with 5 dB between contours in figure 3.14.

3.6 Modelling of the data collection system

Offset

For application of our model, offset is defined as distance from axis $r=0$ to first receiver position. It is standard input and follows from equation (78). Offset is set to be 155.25 m, see figure 3.11.

Source array

As the total length of each source subarray is 8.65 m which equals approximately 0.28λ at 50 Hz, we will approximate each subarray as a monopole. The source array is readily modelled by application of the previously derived three-dimensional capabilities of our numerical model. The source array is aligned with the axes $\theta=0$, $z=7.5$ m, the center subarray on the axis $r=0$.

Receiver array

The hydrophone group separation, 50 m, sets an upper limit on observable nonaliased horizontal wavenumber: approximately 0.06 m^{-1} . Our modelling of the receiver array approximates the actual array by computing a 4096 element array with hydrophone spacing 0.79 m. This array is divided into 64 subgroups, each subgroup consists of 64 hydrophones with spacing between hydrophone groups also equal to 0.79 m. Application of equations (77) with hydrophone separation 0.79 m gives the total range of horizontal wavenumber to be 8.855 m^{-1} . It is thus sufficient to compute a horizontal wavenumber spectrum ranging from approximately zero to 0.12 m^{-1} and set the region ranging from 0.12 m^{-1} to 8.855 m^{-1} equal to zero.

As previously mentioned, the receiver array consists of 52 hydrophone groups, each again consisting of 64 hydrophones. The approximations assume: each hydrophone group to consist of 64 equispaced elements as opposed to the two 32-element groups spaced 3 m apart of the actual array, that the separation between groups is 0.79 m as opposed to 3 m and that the array consists of 64 as opposed to 52 hydrophone groups. These approximations are not considered to be of significant consequence, because, as demonstrated in figure 3.13, the role of this hydrophone clustering is to create a spatial low pass filter with

first minimum at approximately 0.12 m^{-1} .

The reasons for making these approximations is to secure that the width of the horizontal wavenumber bins remain unchanged and that all energy represented by the original horizontal wavenumber spectrum is included in the modelled response.

The sequence for modelling of receiver array is:

- for each of 128 frequencies:
 - compute 64 point horizontal wavenumber spectrum from 0.- to 0.12 m^{-1}
 - preweight according to (78)
 - include zeroes up to 4096 points corresponding to horizontal wavenumber 8.855 m^{-1}
 - perform 4096 point FFT over preweighted K-spectrum
 - postweight according to (78)
- include zeroes in frequency bins 128 to 255
- 256 point FFT over all frequencies
- take real part
- summation over 64 hydrophone groups, each with 64 hydrophones
- inverse postweighting according to (78)
- 64 point FFT over X-direction
- 256 point FFT over T-direction

Figure 3.14 shows an F-K diagram for the same test case that we have investigated previously, except for that the source- and array configuration is modelled as described here. It becomes clear that the effects of source- and receiver geometry is to emphasize the continuous region of the F-K domain. This is obviously an advantage for the seismological purposes for which the system is designed, as it directs energy down into the ocean bottom.

As we described in the chapter on data collection system response, the effect of the source array is to produce a downward propagating main lobe.

3.7 Geoacoustical background information

From [19] we take the following which shows the prior known geoacoustical background information available for the area in which our shots have been recorded:

layer number 1:

	water
compressional wave vel. (m/s)	1475-1485
density (kg/m ³)	1000
thickness (m)	50-100

layer number 2:

age	jurassic-triassic ¹
sediment & rock type	shale-sandstone
compressional wave vel. (m/s)	4200-4800
shear wave vel. (m/s)	2100-2400
compressional wave attenuation (dB/λ)	0.3-0.8
shear wave attenuation (dB/λ)	1.0-2.8
density (kg/m ³)	2450-2650
thickness (m)	800-1000

layer number 3:

age	triassic
sediment & rock type	shale sandstone
compressional wave vel. (m/s)	5100-5500
shear wave vel. (m/s)	2250-2750
compressional wave attenuation (dB/λ)	0.1-0.5
shear wave attenuation (dB/λ)	0.3-1.9
density (kg/m ³)	2.65-2.75
thickness (m)	800-1200

layer number 4:

age

sediment & rock type

compressional wave vel. (m/s) 5800-

shear wave vel. (m/s) 2800-

compressional wave attenuation (dB/ λ)

shear wave attenuation (dB/ λ)

density (kg/m³) 2800-

thickness (m)

¹ can be partly covered by 0.3-3 m of till, glaciomarine sediments or
Holocene mud

3.8 Identification- and modelling of events in the measured data

F-K diagrams for shots numbered 1, 52, 100 are shown in figures 3.15 to 3.17 respectively. As the sailed distance between each shot is 50 m, the distance from first to second and third plot is 2.5- and 5 km respectively.

Before going into a more detailed analysis, we would like to note the resemblance between the three figures, which of course suggests that the parameters which govern propagation in the water layer are basically the same within this 5 km stretch. As a consequence, the environmental parameters we may identify are relatively valid for at least this area. It is in all figures possible to identify the 0., 1., 2. and 3. mode. It is also possible to identify aliased energy in the 0.12 m^{-1} to 0.24 m^{-1} horizontal wavenumber region, especially in figure 3.17. This will be more commented on and exploited.

3.8.1 First approximation

We will now, having established a framework for understanding some of the features of the F-K plot, proceed to attempt to interpret the F-K diagrams for the three shots we have presented. We will concentrate our attention on the first shot, shown in figure 3.15.

We will start out by determining the average velocity for compressional waves in the water layer. As we already know from a previous section, the phase velocity of a mode will approach the water velocity asymptotically from above, the group velocity will approach the water velocity asymptotically from below, and hence the tangent of a mode at "high" F-K values represents the water velocity. From figure 3.15, a trained eye can observe that the 1. mode is spatially aliased and thus continues from approximately $\{0.30\}$. The contour plot of

figure 3.15 is shown in figure 3.18 where a line marker for 1466 m/s passing through {0.12,28} is drawn, also for the spatially aliased region. The first mode lies above the line marker: its phase velocity is greater than 1466 m/s and its group velocity (slope) has a lower value than that of the line marker's 1466 m/s. It should now, if necessary, be easier to identify the aliased 1. mode in the surface plot of figure 3.15.

We should also notice that the 1466 m/s line marker crosses the 0. mode close to its peak. As we know, this peak is an effect of both the medium and the source geometry, so we will not draw any firm conclusions based on the peak. We notice, however, that the asymptotic phase velocities are above the line marker at low frequency-wavenumbers in accordance with the previously described testcase. The 0. mode will be looked into in the following.

The line marker in figure 3.18 passes through {0.12,28} in the F-K plot. The points {0.12,27.5} and {0.12,28.5} correspond to phase velocities 1440 m/s and 1492 m/s respectively ($\pm 1.8\%$). These points are in the order of reasonable observation accuracy. Obviously, this is not a very accurate method for determining ocean sound speed velocity by the underwater acoustician's standards.

We now proceed to estimate the cut-off frequencies for the 1., 2. and 3. mode. This is found to be done simplest by using a ten-point divider along the frequency axis. With point 0 at the origin, point 1 at the 1. mode, point 3 at the 2. mode and so on, we arrive at an estimated cut-off frequency for the 1. mode to be 7 Hz. Inserting this value and the phase velocity for compressional waves in the water layer, 1466 m/s, in equation (92), yields a water depth of 52.3 m.

The surface plot in figure 3.15 shows two very distinct peaks in the 1. and 2. mode. These peaks are partly a result of the source geometry, but they are much sharper than the lobes of the source diagram, see figure 3.13. We take these peaks to be at the phase velocity of the compressional wave in the ocean bottom and draw a line

through them as shown in figure 3.19. Again, the accuracy is limited, but if we accept the point $\{0.1189, 70\}$ (1), we arrive at 3700 m/s.

Estimation of the ocean bottom shear wave velocity is not quite so straightforward as the other quantities. If the data were not "contaminated" with the source array structure, and also if the hydrophone spacing were closer so that we could observe a higher horizontal wavenumber unaliased, we could look for the "point(s)" where the F-K response rises up and becomes discrete and also perhaps for the point(s) where the group- and phase velocities are equal. As this is not the case here, we shall have to rely more heavily on the information the 0. mode may be able to yield.

An estimate of the Rayleigh- and Scholte wave velocities for the ocean bottom is indicated by the line markers in figure 3.10. It must be appreciated that the determination of these quantities is rather subjective.

The Rayleigh- and Scholte wave velocities for some values of shear velocity, computed as described in appendix 1, is shown in table 1. The compressional wave phase velocities for water and bottom are those that we have arrived at: 1466 m/s and 3700 m/s and the density of the ocean bottom is assumed to be 2500 kg/m^3 .

shear [m/s]	p. Rayleigh [m/s]	Scholte [m/s]
1200	1137	1137
1400	1322	1322
1600	1503	1377
1800	1682	1370
1850	1726	1368
1900	1768	1364
1915	1780	1363
1950	1811	1362
1990	1844	1358
2000	1853	1358

Table 1: Computed values of pseudo-Rayleigh- and Scholte wave velocities vs. shear velocity.

From table 1, we see that for shear velocities greater than the water velocity, it is the pseudo-Rayleigh velocity that is mostly influenced by variations in sound speed. All the computed Scholte wave velocities lie higher than 1204 m/s as estimated in figure 3.20. We will for the time being assume the shear velocity of 1915 m/s which matches the estimated pseudo-Rayleigh velocity, 1780 m/s figure 3.20. The line marker for 1915 m/s passing through {0.12, 36.57}, seems to be somewhat too low for the group velocity to equal the phase velocity in the 1. mode. This is not possible to determine with certainty, but it would seem that a somewhat higher shear velocity: in the order of 1990 m/s, passing through {0.12, 38} in figure 3.21, would give a better fit to the 1. mode. This implies a pseudo-Rayleigh velocity of 1844 m/s (from table 1) passing through {0.12, 35.2} which is acceptable when adopted to shot number 1 figure 3.21.

The geoacoustical model presented in chapter 3.7 suggests higher compressional- and shear velocities in the first bottom layer: 4200-4800 m/s and 2100-2400 m/s respectively. The same bottom type, shale-sandstone, may according to appendix 2, however, have compressional- and shear velocities in the range 2100-4800 m/s and 1200-2400 m/s respectively. The estimated values should thus be well within geological acceptable bounds.

We do not see any feasible criteria for determination of ocean bottom density and will, based on the geoacoustical model on chapter 3.7, assume it to be 2500 kg/m^3 . The losses will not be considered quite yet.

Summarizing, we have arrived at the following conclusions for a first approximation to the environmental data governing shot number 1.:

compressional wave phase velocity in water:	1466 m/s
compressional wave phase velocity in bottom:	3700 "
shear wave phase velocity in bottom:	1990 "
water depth:	52.3 m
density of bottom (assumed):	2.5 kg/m^3
attenuation of comp waves in bottom (assumed):	2 dB/ λ
attenuation of shear waves in bottom (assumed):	2.5 "

Line markers indicating these velocities and also corresponding pseudo-Rayleigh- and Scholte velocities; are shown in figure 3.21.

The modelling of this 1. approximation to shot number 1 with simulation of source- and receiver system included and excluded is shown in figures 3.22 and 3.23 respectively.

3.8.2 Second approximation

In comparing figure 3.22 with figure 3.15, the most striking discrepancy is to be found in the continuous region where the model predicts a much higher level than what is seen in the measured data. We have seen from figures 3.13 and 3.14, that the main influence of the source and receiver geometry is to emphasize this continuous region. For the model input data, we have appreciable impedance contrast between water and bottom. It is thus in no way unreasonable that the model should predict this response in the continuous region. We must therefore look into what effects of the medium we have not taken into account. We will consider the following hypothesis:

- the source-streamer geometry is not according to specifications
- wrong density in the bottom
- wrong attenuation in the bottom
- sloping bottom
- rough bottom
- an added bottom layer with high attenuation

An erroneous source-streamer geometry could conceivably be such that the source's main lobe is distorted to be in the horizontal wavenumber region where the pronounced spikes occur, approximately 0.01 m^{-1} to 0.04 m^{-1} . I do not wish to speculate on the likeliness of this hypothesis, as we do not have any information to support it.

We have in our model assumed an ocean bottom density of 2500 kg/m^3 . Decreasing the reflection coefficient at the ocean bottom would imply reducing the density, see figure 3.8. The absolute lowest acceptable value is 1000 kg/m^3 , otherwise the bottom would float up (!). Modelling of reduced densities have shown that it is not sufficient to account for the difference between model and measurement.

Figures 3.9 and 3.10 show that the reflection coefficient in the continuous region is not affected by variation of losses in the ocean bottom. Therefore the hypothesis of wrong attenuation in the bottom cannot be accepted.

Comparison of the F-K diagram for shot numbers 1, 52 and 100, figures 3.15, 3.16 and 3.17, show that they grossly resemble each other, consequently a steep sloping bottom is not likely.

For the frequency regions of the F-K diagram we are considering, the wavelength of compressional waves in water is in the order of 50 m and more. As we have arrived at a water depth in the order of 52 m, it is not likely that there can be bottom roughness on a scale sufficient to produce the reduction in continuous region response we are looking for.

Beside the possibility of a weakly sloping bottom, we are left with the last hypothesis: an added bottom layer with high attenuation, inserted "on top of" the existing bottom. We should at once be able to postulate some properties this layer should exhibit. As we in our data "see" the bottom we have arrived at, the layer should be transparent in the sense that the impedance contrast between water and attenuating layer is almost negligible. Its density must of course be greater than that of the water.

Conversion of energy to shear waves cannot play an important role in the continuous region as the particle velocity of the incident waterborne wave is close to normal to the boundary. A shear wave would have to be downward refracted and hence have its dominant particle motion parallel to the boundary.

The lowest line marker in figure 3.23 is set at 1358 m/s which is the computed Scholte wave velocity for this situation (refere to table 1). The 0. mode's phase velocity is above this value, but it is in the process of reaching it asymptotically. We remember from figure 3.20, however, that we have estimated the asymptotic value for the 0. mode

to be at most 1204 m/s. For our situation where the bottom shear velocity is greater than the compressional wave phase velocity in water, it is this water velocity that has significant influence on the Scholte wave velocity. We will choose to try a compressional wave velocity in the attenuation layer to be less than in water, for thereby "pulling down" the Scholte wave velocity at the lower substrate layer.

The geoacoustical model in chapter 3.7 allows for a 0.3 - 3 m thick layer of till, glaciomarine sediments or Holocene mud. Appendix 2 indicates that clay exhibits compressional- and shear velocities in the region 100-2500 m/s and 200-1000 m/s respectively. I would also like to add that I have participated on experiments conducted by NDRE from the research vessel H U Sverdrup in the same area. When we recovered equipment from the ocean bottom, it was partly covered by a blue clayish substance.

Based on this discussion, we will introduce a thin layer with high attenuation and acoustical impedance equal to water. The environmental parameters for the 2. approximation to shot number 1 will be as shown in figure 3.24.

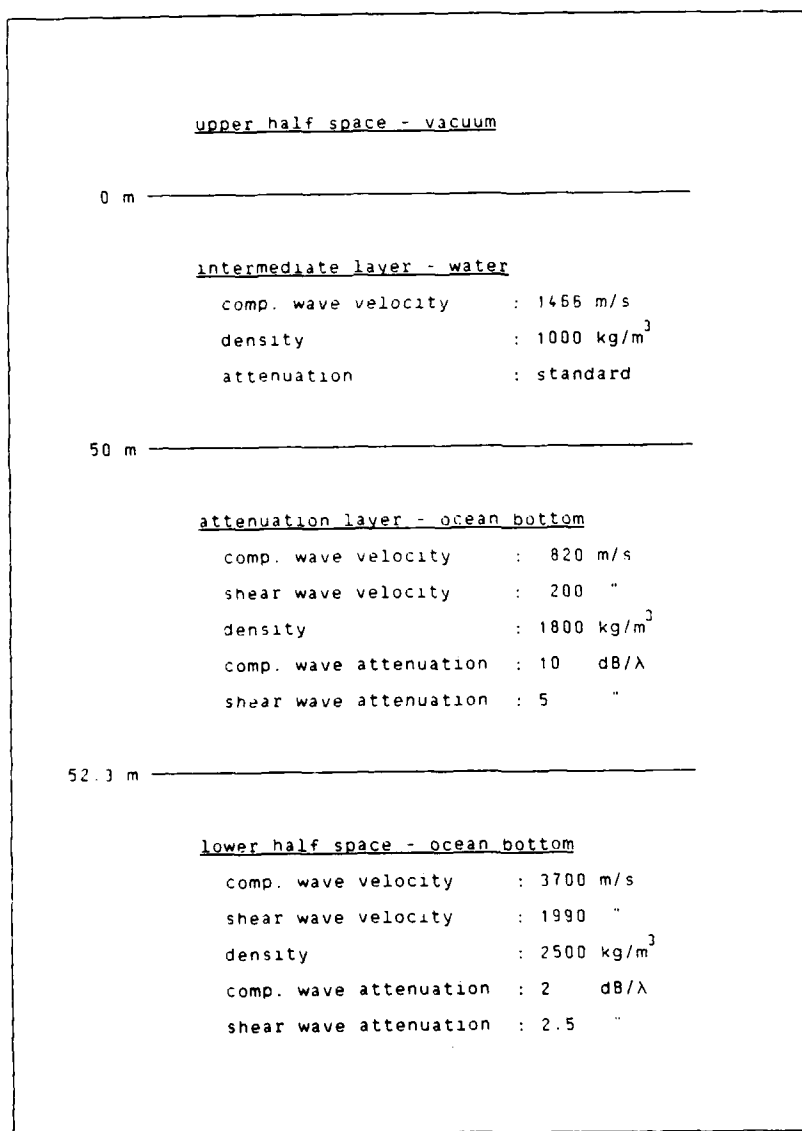


Figure 3.24 Environmental parameters for 2. approximation to shot number 1.

The losses we have assumed for the attenuating layer are far higher than what is to be expected in known bottom types [19], but they have been exaggerated in order to see if attenuation on this scale, whatever physical explanation they may have, could account for the observed low response in the continuous region.

3.9 Discussion of fit between measurement and model

F-K diagrams for the 2. approximation with environmental data as shown in figure 3.24, including- and excluding simulation of source-streamer geometry are depicted in figures 3.25 and 3.26 respectively.

Comparing the F-K responses with and without attenuation layer, figures 3.26 and 3.23, we can see that the attenuation layer has had the effect of reducing the continuous F-K region response, but as can be seen from the F-K response for the 1. approximation when we simulate the source-receiver geometry, figure 3.25, we still have a far too strong F-K response in the continuous region. Figures 3.27 to 3.32 show reflection coefficients and bottom impedances when the parameters of the attenuating layer are perturbed. We notice that shear wave-velocity, -attenuation, and density do not affect the module of reflection coefficient in the continuous region. Consequently, the applied shear parameters are not of significant importance in the continuous region. From figure 3.32, compared with figures 3.27 and 3.30, it is seen that on a relative basis, it is layer thickness and thereafter compressional wave-velocity and attenuation that have influence on the continuous region response.

Again, comparing the F-K response with and without the attenuating layer, figures 3.26 and 3.23, we see that the attenuating layer has reduced the spike also at the phase velocity equal to compressional wave velocity in the substrate layer.

Obviously, we have not reached a solution with a perfect fit between measurement and model, especially on a relative quantitative scale. I do feel, however, that there is some success on a qualitative scale: the water, bottom P- and S- velocity parameters have been observed and interpreted in the measured data and their effects in the sense of loci of modes, successfully modelled. Compressional wave velocities manifest themselves clearly. The shear wave velocities, although they

have a more obscure manifestation, are collaborated by several indicators (group velocity equal to phase velocity for higher order modes, pseudo-Rayleigh and Scholte wave velocities for 0. model).

We have not been able to verify that the assumptions on which our numerical model is based upon, are fulfilled.

The question of uniqueness of solution has not been addressed here. The lobe structure in the measured F-K data have been attributed to the side lobe structure of the source array. Further modelling, not reported here, has shown that such a lobe structure may be caused by multiple reflections within a bottom layer: inter bottom layer resonance. If the second bottom layer has a greater P-wave velocity than the first, P-waves may be coupled from the water into the first layer and experience total reflection at the boundary between 1. and 2. bottom layer. This effect can manifest itself as resonance peaks in the region where the horizontal phase velocity is between the P-wave velocities of 1. and 2. bottom layer. This hypothesis has not been considered, as we have to account for the effect of source sidelobes, which are in reasonable agreement with the observed lobes. Consequently, a combination of F-K- and time- domain methods together with a monopole source, may prove an advantage in solving uniqueness problems.

It is concluded that this work indicates that it is possible, for situations with occurrence of "many" multiple surface-bottom reflections, to infer ocean bottom P- and S- wave velocities from near surface measurements.

3.10 Suggestions for future work

For future work, I would first of all like to see data from a similar experiment, but with a different source-streamer geometry. The source should be a monopole. This in order not to emphasize the low horizontal wavenumber region and also to avoid sidelobe contamination. This would readily resolve the question of whether the lobes observed in the measured data are caused by source sidelobe structure or inter bottom layer resonance. A similar subarray of the type used in the data we have examined here should suffice. It is of course necessary to look into the aspect of source level and signal to noise ratio. For the streamer we should have closer hydrophone spacing so as to be able to achieve a greater unaliased horizontal wavenumber. It would be an advantage to repeat the experiment in the same general area. If another area were to be chosen, one should seek a flat hard homogeneous bottom so that the horizontal stratification assumption of the model is fulfilled and also such that we have "many" multiple reflections, i.e. a high Q resonator which consequently shows a pronounced mode structure.

One should further be aware of the water depth, such that the number of modes is within practical limits.

One should, in a possible continuation of this work, look into the feasibility of combining time- and F-K- domain methods, perhaps in an alternating iterative manner.

Automatic numerical iteration of model output to match measurement may be undertaken in the future, but initial settings of the model must, in my opinion, be carried out prior to numerical iteration.

A future experiment should have the capabilities of ensuring that the assumptions on which the model is based, are fulfilled.

4 CONCLUSIONS

A numerical model of wave propagation in horizontally stratified media has been presented. The model is based on FFP-, global matrix- and angular expansion techniques. The solution is exact, except for a cylindrical region in which center axis and source(s) are included.

Shot data, collected by a seismic survey configuration consisting of a source array and a streamer is presented. Limitation in system response imposed by source-streamer geometry is discussed and modelled.

The effects of environmental parameters on events observed in measured data are analyzed and modelled in the F-K domain. The fit between model and measurement compares for location of modes, but not completely on a relative-quantitative scale. Uniqueness of estimated environmental parameters is discussed, but not proved. The F-K methods applied here should be supplemented with other methods, possibly time domain methods.

A future experiment with monopole source and closer streamerhydrophone separation should be carried out. It should preferably take place in the same area, or in a similar area which is horizontally stratified with multiple reflections, and a depth so that the number of modes is within practical limits. Core samples are suggested for verification of estimated parameters

The methods developed here indicate that, under favourable conditions, is possible to infer ocean bottom parameters such as P- and S- wave phase velocities from near surface measurements.

5 ACKNOWLEDGMENTS

There have been many stimulating discussions throughout the various stages of this work. My close cooperation with Dr. Henrik Schmidt at the SACLANC ASW Research Centre, LaSpezia, Italy is highly appreciated and I must also thank my supervisor Prof Jens Hovem, cosupervisor Erik Sevaldsen, Prof Andreas Tønning, Dr Tor Knudsen, Knut Sørstrand, Even Lunde and Trond Jensenrud. Per Riste has been of great help in demultiplexing the seismic data and the most significant effort on the part of Helge Herheim in programming the interactive graphics program involved, is also highly recognized and appreciated.

I am greatfull to the Norwegian Petroleum Directorate for supplying- and giving consent to publish the shot data.

The financial travel support given by the Royal Norwegian Council for Scientific Research is highly acknowledged, as this project would not have been possible without.

The solid support and patience given by my employer the Norwegian Defence Research Establishment through the directors Finn Lied and Erik Klippenberg and division heads Inggald Engelsen and Jarl Johnsen is also highly acknowledged.

6 REFERENCES

- [1] W M Ewing, W S Jardetzky and F Press, Elastic Waves in layered media (McGraw-Hill, New York, NY, 1957)
- [2] H W Marsh, M Shulkin and S G Kneale, "Scattering of underwater sound by the sea surface," J Acoust Soc Am 33, 334-340 (1961).
- [3] W T Thomson, "Transmission of Elastic Waves through a Stratified Solid Medium," Journal of Applied Physics, Vol 21, 89-93 (1950).
- [4] N A Haskell, "The Dispersion of Surface waves on Multilayered Media," Bulletin of the Seismological Society of America, Vol 43, 17-34 (1953).
- [5] F R DiNapoli and R L Deavenport, "Theoretical and numerical Green's function solution in a plane multilayered medium," J Acoust. Soc Am 67, 92-105 (1980).
- [6] F R DiNapoli, "Fast field program for multilayered media," Rep 4103, US Naval Underwater Systems Center, New London, CT (1971).
- [7] H W Kutschale, "Rapid computation by wave theory of propagation loss in the arctic ocean," Rep CU-8-73, Columbia University, Palisades, NY (1973).
- [8] C H Harrison, "Modelling Low Frequency Sound Propagation in Solid/Fluid Layers," Acoustics and The Sea-Bed, Bath University Press, Bath, UK (1983).

- [9] H Schmidt and F B Jensen, "Efficient numerical solution technique for wave propagation in horizontally stratified ocean environments," Rep SM-173, SACLANT ASW Research centre, LaSpezia, Italy (1984).
- [10] H Schmidt and S Krenk, "Asymmetric vibrations of a circular elastic plate on an elastic half-space," Intern Journ. of Solids and Structures, 18, 91-105(1982).
- [11] P M Morse and K U Ingard, Theoretical acoustics Mc Graw-Hill, New York, NY(1968).
- [12] Andreas Tønning, Personal communication
- [13] J A Stratton, Electromagnetic Theory Mc Graw-Hill, New York, NY(1941).
- [14] J A Hudson, The excitation and propagation of elastic waves, Cambridge University press 1980
- [15] P M Morse and H Feshbach, Methods of theoretical physics Theory Mc.Graw-Hill, New York, NY(1953).
- [16] A Tønning, Lecture notes on ultrasonic waves in crystals
- [17] K Aki and P G Richards, Quantative Seismology Theory and methods, W H Freeman and company San Franscisco 1980.
- [18] D Rauch, Seismic interface waves in coastal waters: A review, SACLANT ASW Research centre report SR-42 1980.
- [19] J I Faleide, Geoacoustic modeling of the sea floor- with examples from the Barents sea, North Sea, Skagerak, Kattegat and Oslofjord

Appendix 1: Rayleigh- pseudo-Rayleigh and Scholte waves

From D Rauch [18], we take the following equation for determination of Rayleigh- and Scholte wave velocities at a boundary between a solid and vacuum or fluid respectively.

$$4X(X-1)^{1/2}(X-R)^{1/2} - (2X-1)^2 - H \frac{(X-R)^{1/2}}{(X-N)^{1/2}} = 0 \quad (A-1)$$

where

$$H = \frac{c_w}{c} \quad N = \frac{c_s}{c_w} \quad R = \frac{c_s}{c_c} \quad X = \frac{c_s}{c}$$

and the subscripts w,c,s refer to water, compressional and shear properties respectively and unsubscripted c is the horizontal wave velocity. For the case of vacuum over solid, H, and consequently the last term of (A-1) vanishes.

For both cases the numerical solution is found by stepping X through its possible range and seeking the minimum.

Appendix 2: Geoacoustical properties of various sediment and rock types

Jan Inge Faleide [19] has compiled the following tabel for some geoacoustical properties of various sediment and rock type. He has collected these data from several sources to which he referes collectively.

	P-VELOCITY (m/s)	S-VELOCITY (m/s)	DENSITY (g/cm ³)	DENSITY (aver)
AIR	310- 360			0.0013
OIL	1250-1400		0.60-0.90	
WATER	1400-1550		0.98-1.05	1.025
ICE	3100-4200	1600-2000	0.88-1.07	0.95
CLAY	1100-2500	200-1000	1.50-2.60	2.20
SILT	1400-1800	150- 450	1.80-2.20	1.95
SAND	1000-2000	100- 500	1.60-2.20	1.90
MORaine	1500-2700	500-1300	1.50-2.00	1.80
SHALE	2700-4800	1500-2400	2.00-3.20	2.40
SANDSTONE	2100-4500	1200-2800	2.10-2.80	2.35
CHALK	2100-4200	1000-2000	1.60-2.60	2.00
GYPSUM	2000-3500	1000-2000	2.20-2.60	2.35
ANHYDRITE	3500-5500	2000-3200	2.80-3.00	2.90
SALT	4200-5500	2000-3200	2.10-2.40	2.15
LIMESTONE	3400-7000	1800-3400	2.10-2.90	2.55
DOLOMITE	3500-6900	2000-3800	2.40-2.90	2.75
GNEISS	3500-7500	1700-3600	2.40-3.00	2.75
MARBLE	3750-6950	2000-3800	2.60-2.90	2.75
GRANITE	4750-6000	2400-3800	2.50-2.90	2.65
BASALT	5500-6400	2700-3400	2.70-3.30	3.00
GABBRO	6450-6700	3400-3700	2.70-3.30	3.00
ULTRABASIC ROCKS	7400-8600	3700-4400	3.00-3.40	3.20

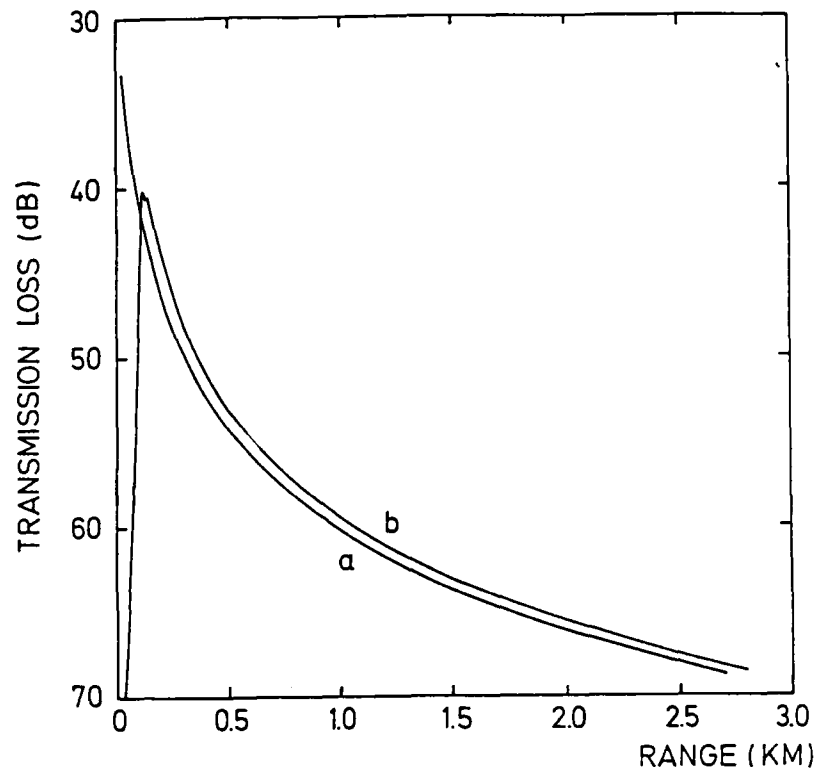


Figure 2.1 Transmission loss for a free space environment, the receiver is located 40 m above the source. A: source at center axis ($r=0$) i.e. two-dimensional case. B: source displaced 100 m in positive x-direction i.e. three-dimensional case.

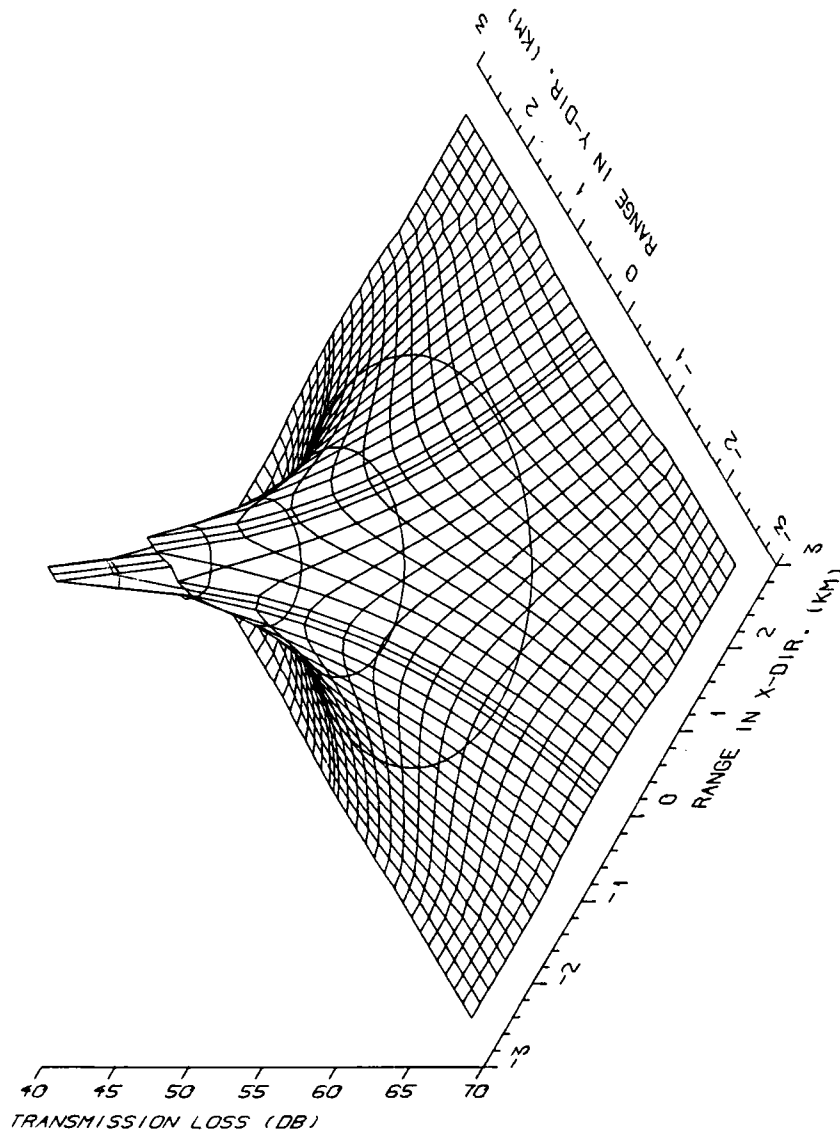


Figure 2.2 Polar plot of transmission loss for a point source in free space, the source displaced 100 m in the positive X-direction.

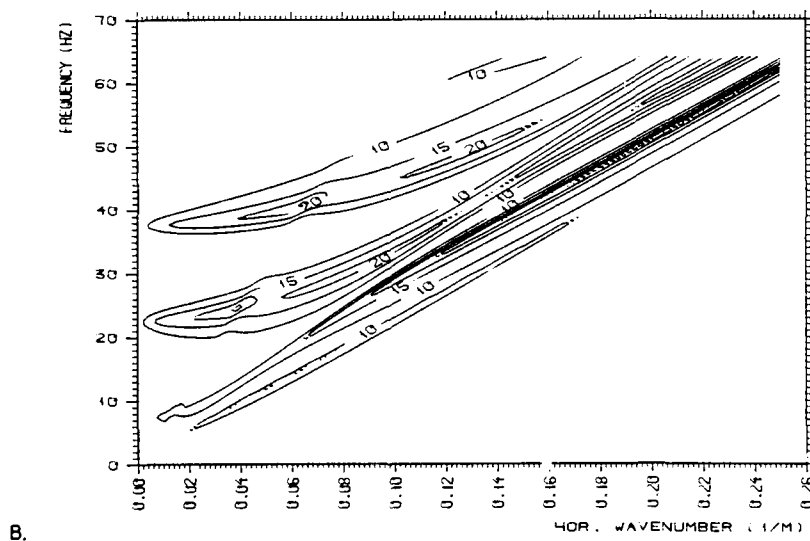
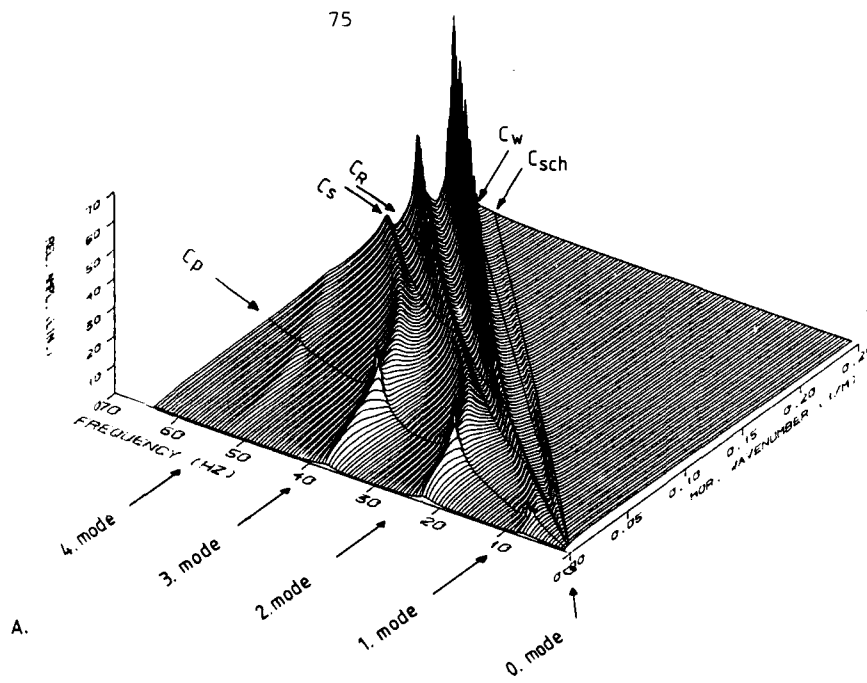


Figure 3.3 F-k diagram for single bottom layer; test case. A: surface plot in linear scale. B: contour plot in logarithmic scale with 5 db between contours. The layer markers indicate velocities of 4000 m/s, 2000 m/s, 1065 m/s, 1500 m/s and 1330 m/s.

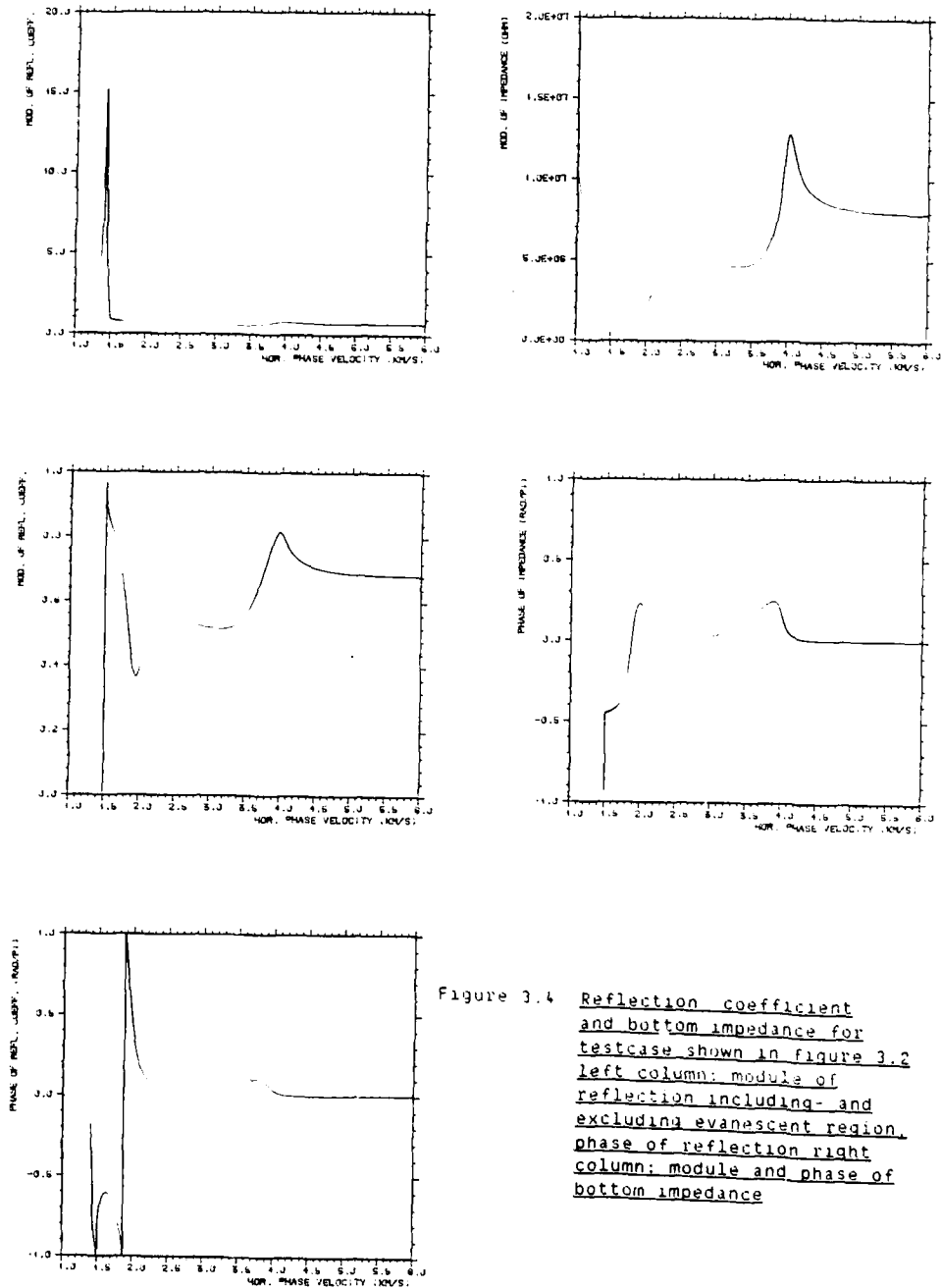


Figure 3.4 Reflection coefficient and bottom impedance for testcase shown in figure 3.2
left column: module of reflection including- and excluding evanescent region,
phase of reflection right column: module and phase of bottom impedance

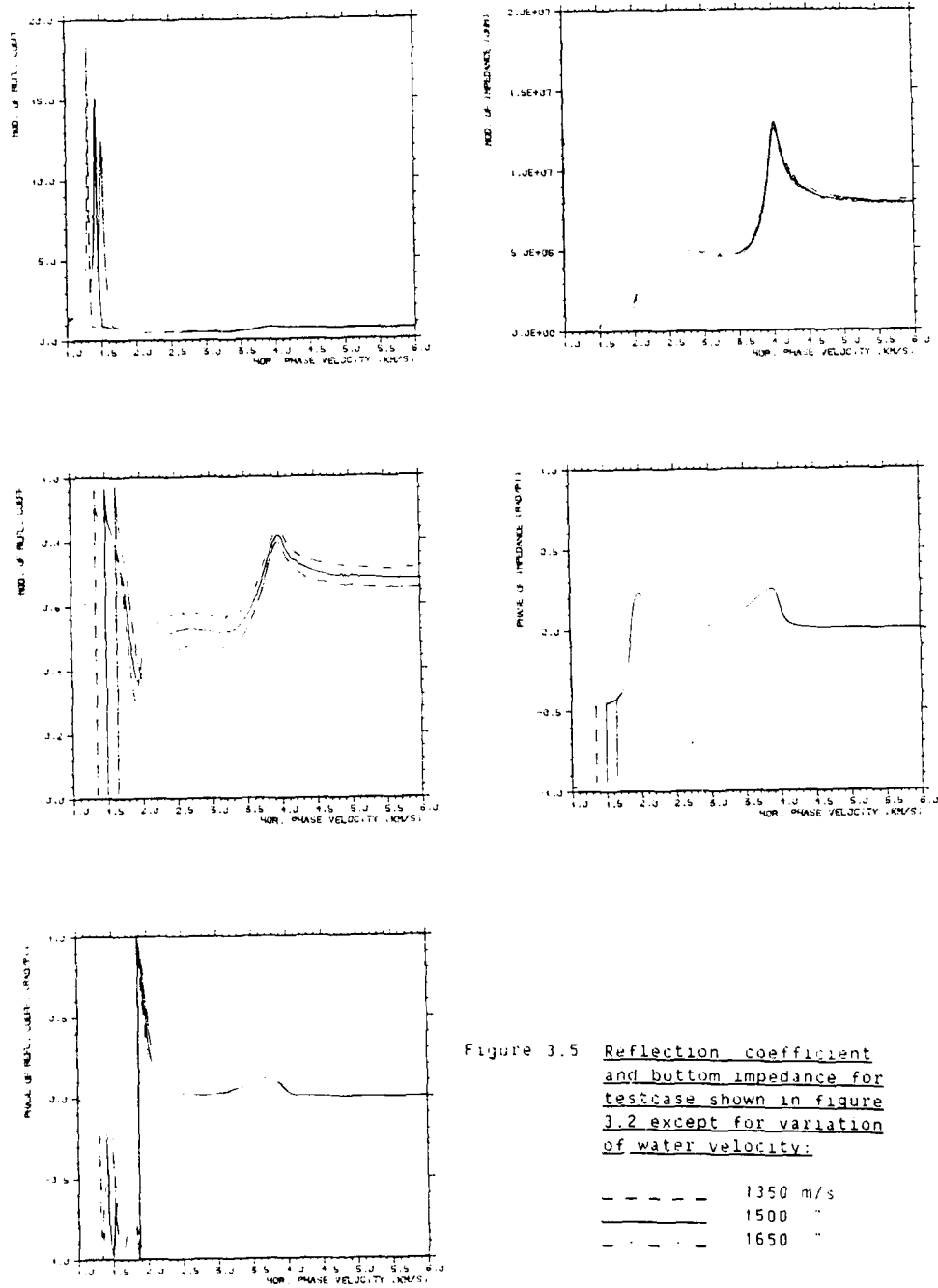


Figure 3.5 Reflection coefficient and bottom impedance for testcase shown in figure 3.2 except for variation of water velocity:

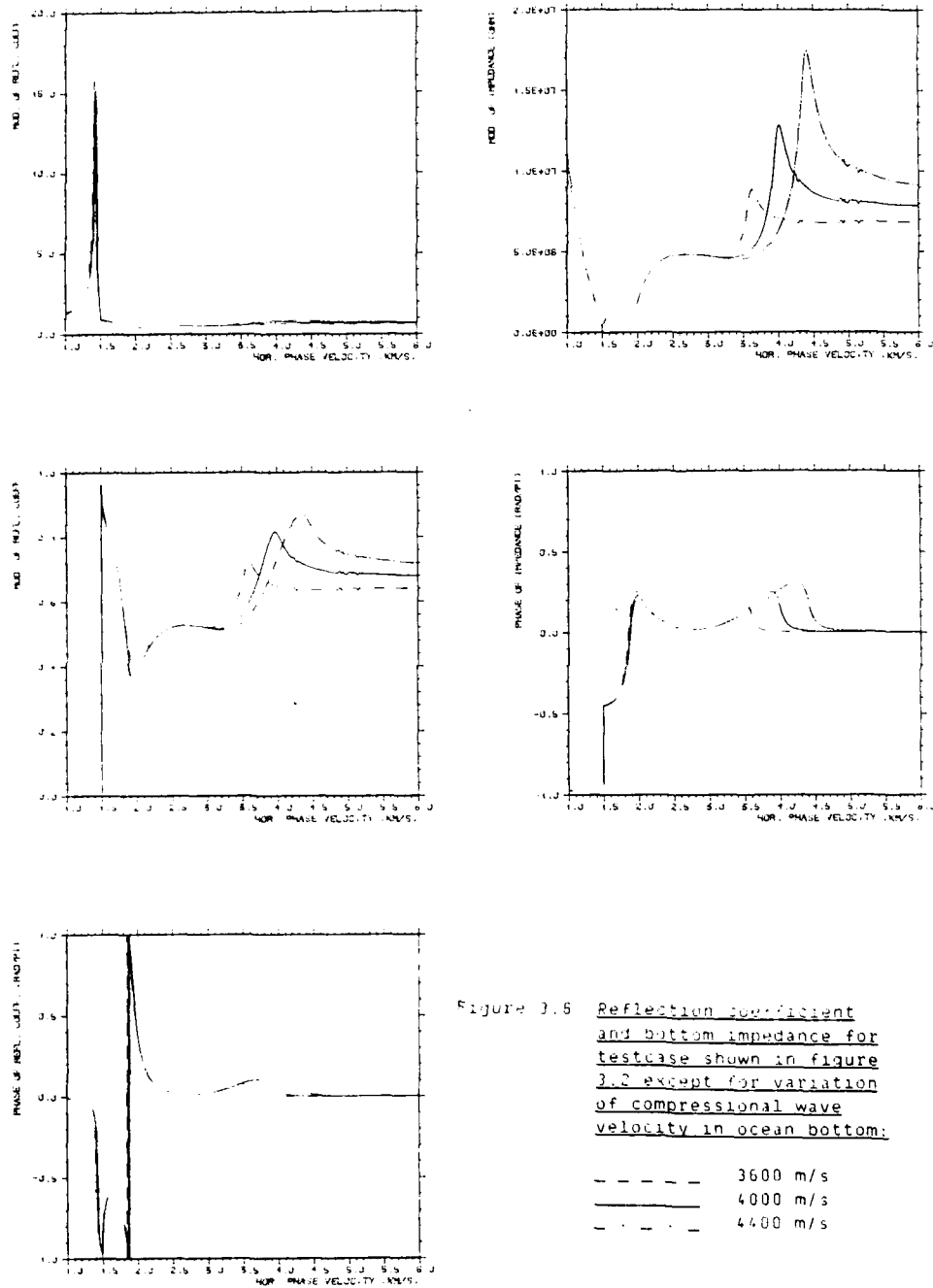


Figure 3.5 Reflection coefficient and bottom impedance for testcase shown in figure 3.2 except for variation of compressional wave velocity in ocean bottom:

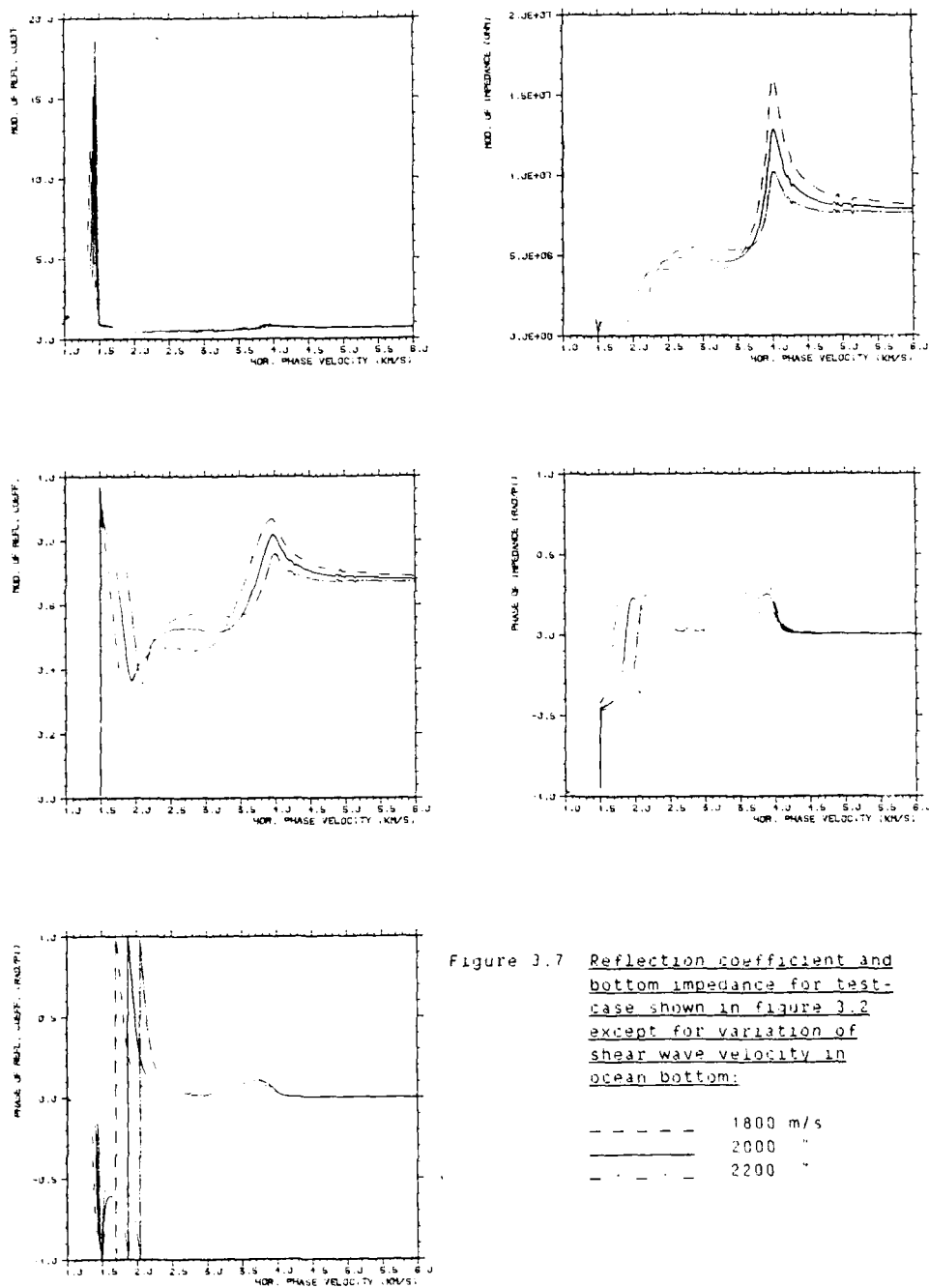
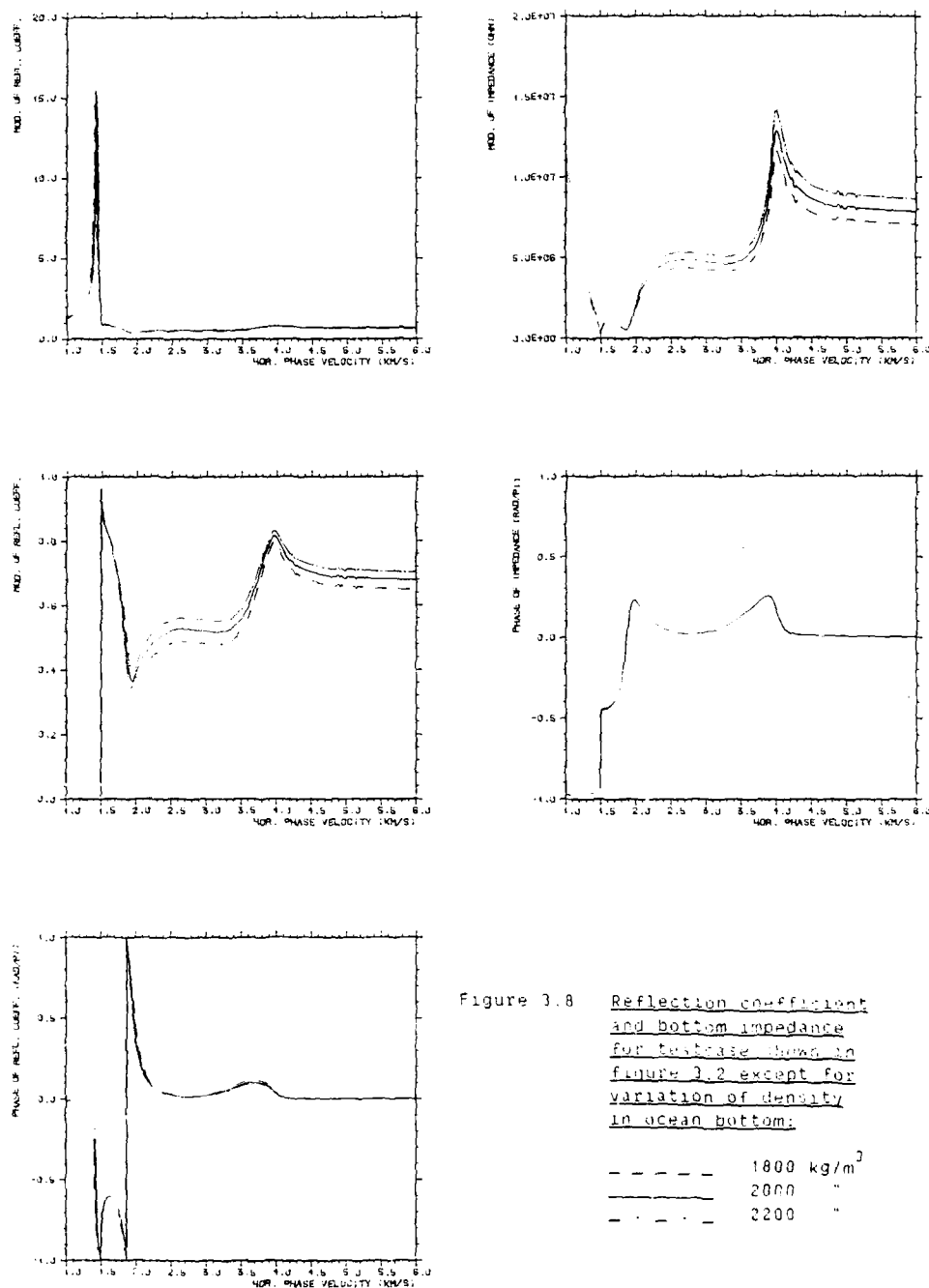


Figure 3.7 Reflection coefficient and bottom impedance for test case shown in figure 3.2 except for variation of shear wave velocity in ocean bottom:



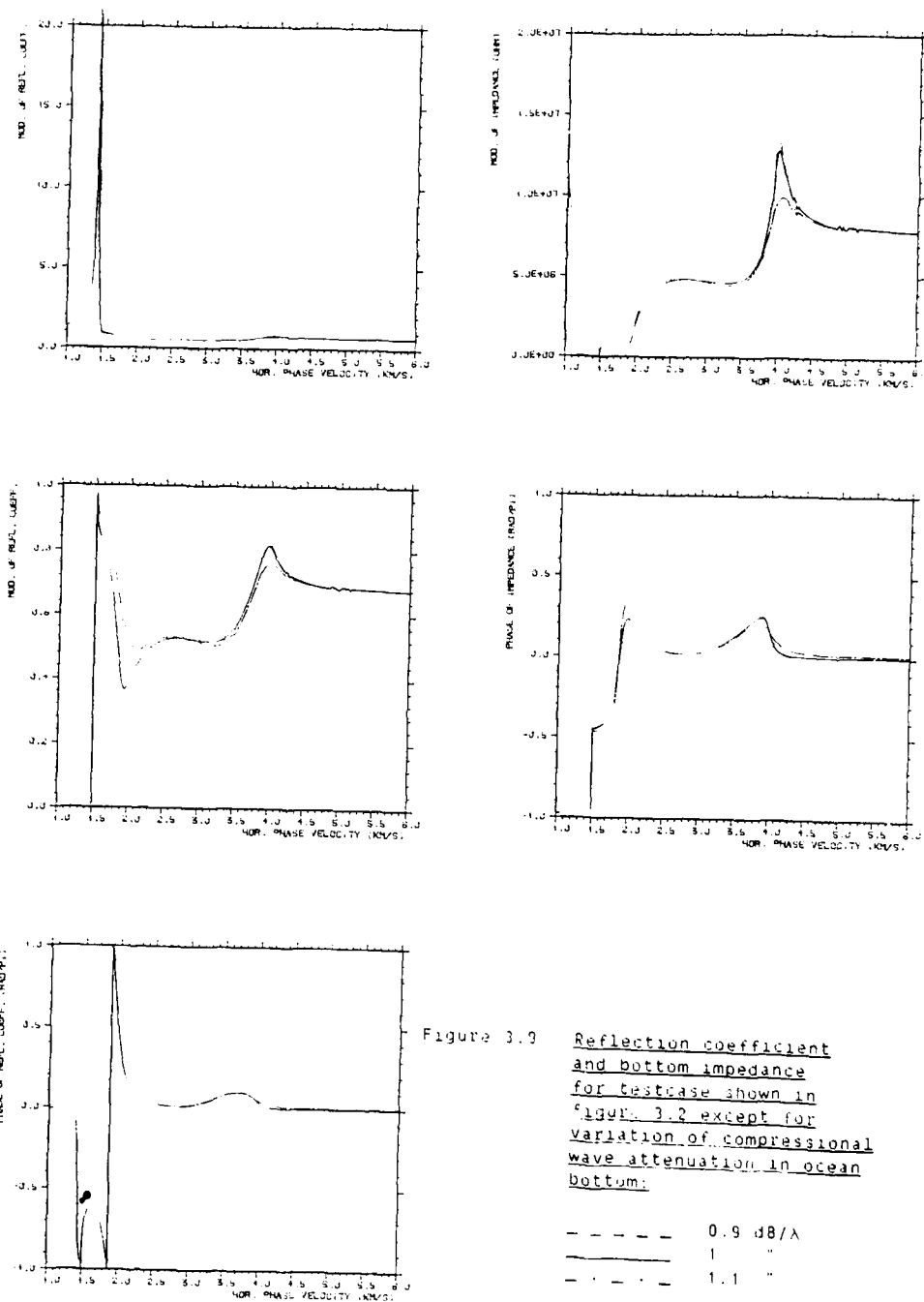


Figure 3.3 Reflection coefficient and bottom impedance for test case shown in figure 3.2 except for variation of compressional wave attenuation in ocean bottom:

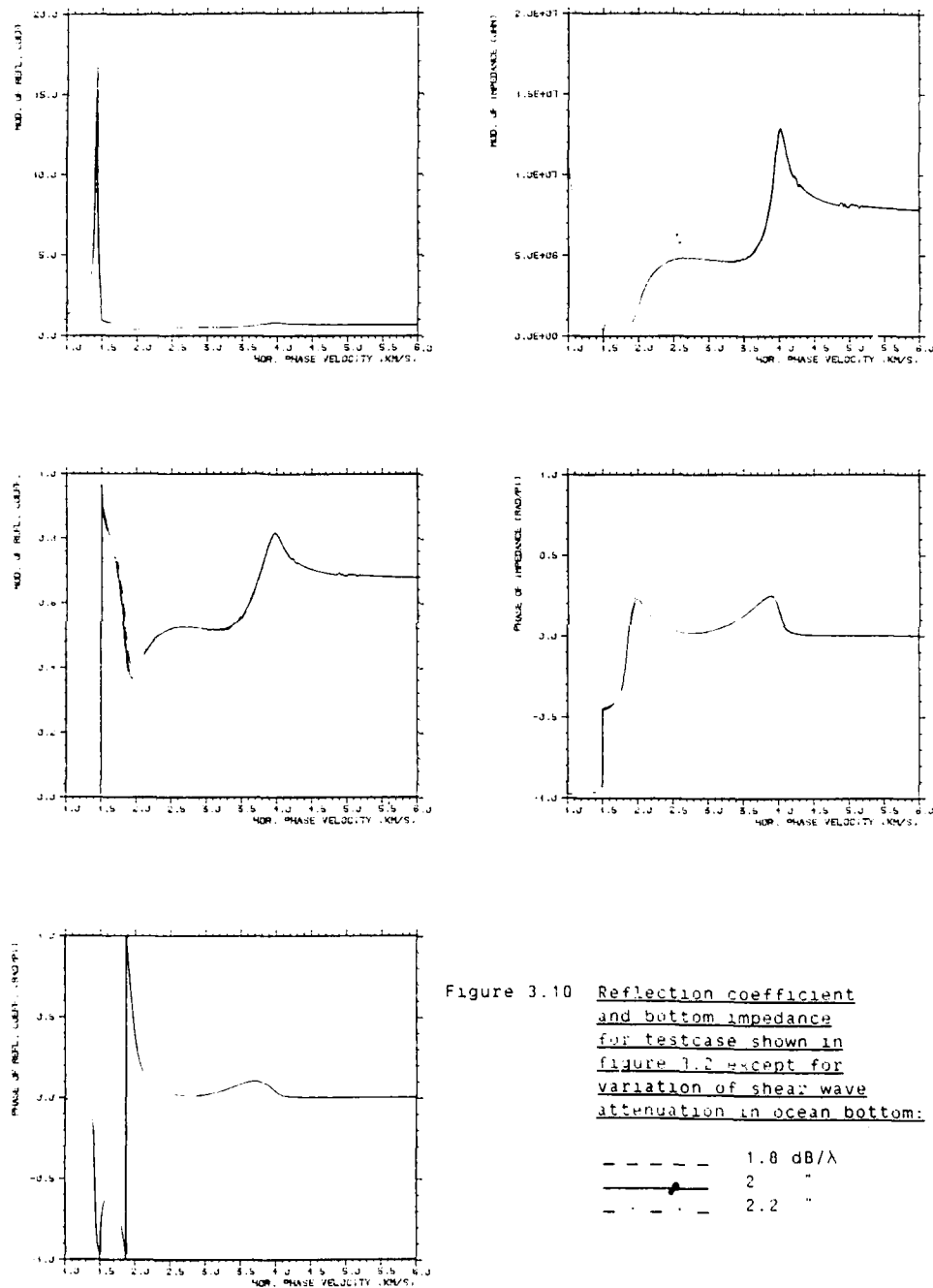


Figure 3.10 Reflection coefficient and bottom impedance for test case shown in figure 1.2 except for variation of shear wave attenuation in ocean bottom:

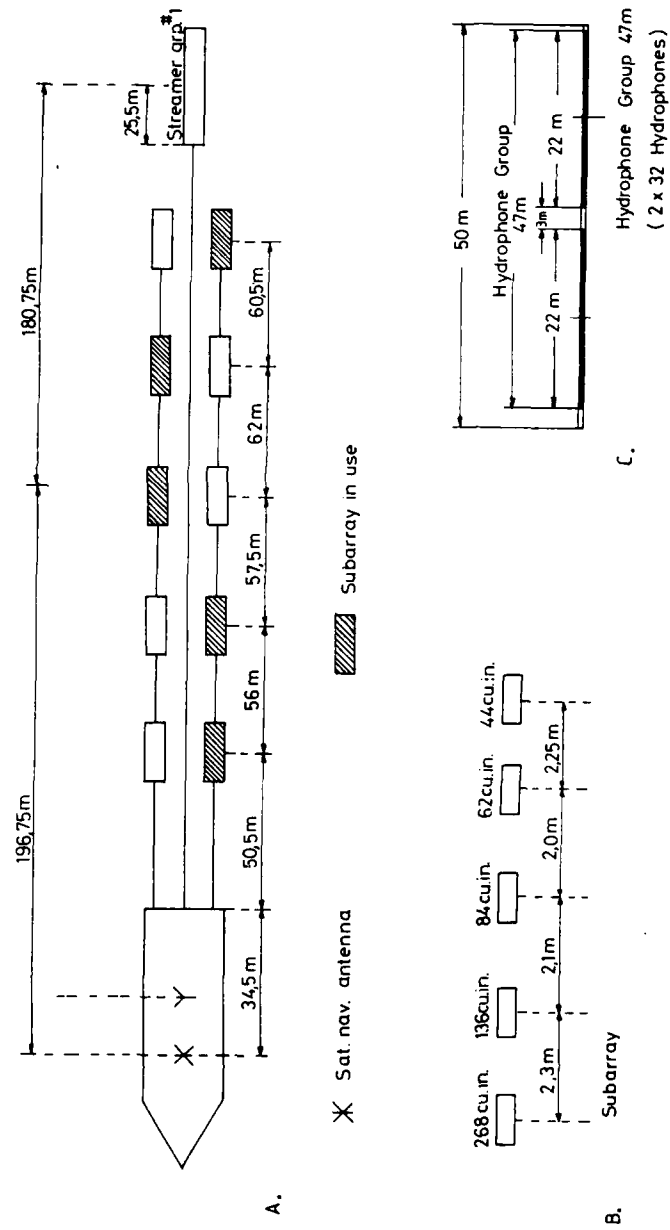


Figure 3.11 Geometry of source and streamer. A: total ship, source and streamer system. B: geometry of subarray. C: geometry of hydrophone subgroup.

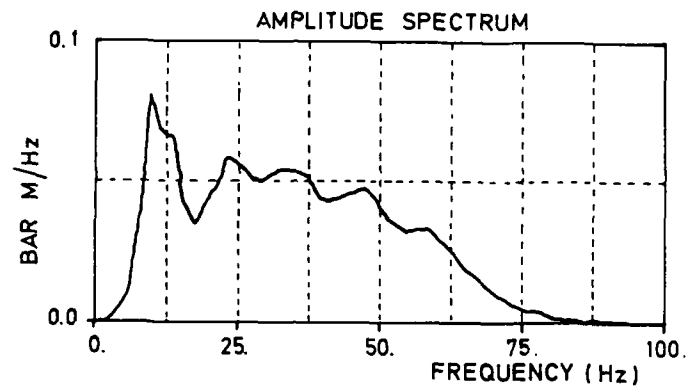
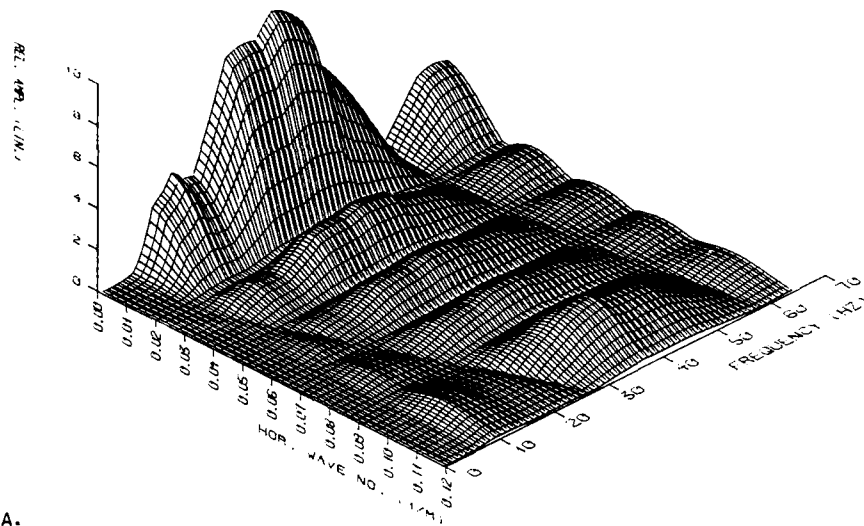
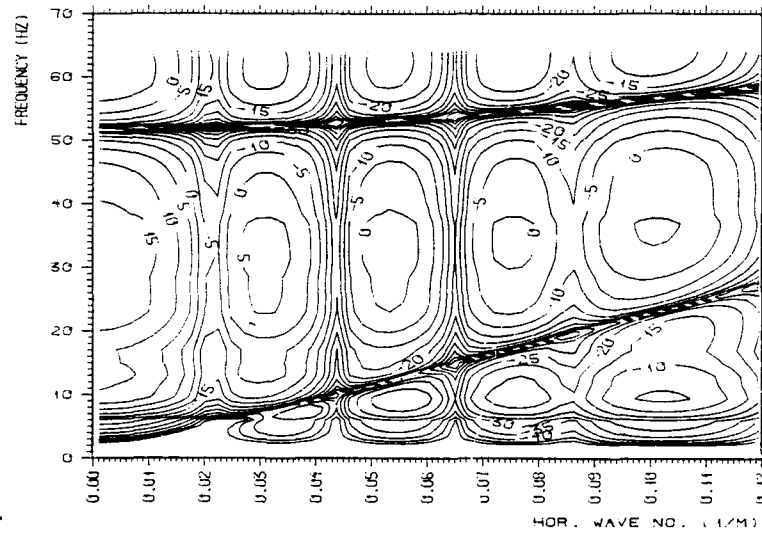


Figure 3.12 The frequency spectrum of the source. (from NPD)

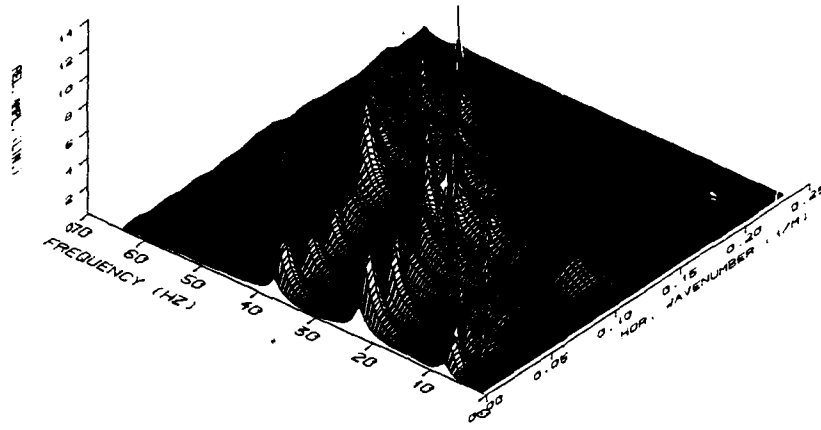


A.

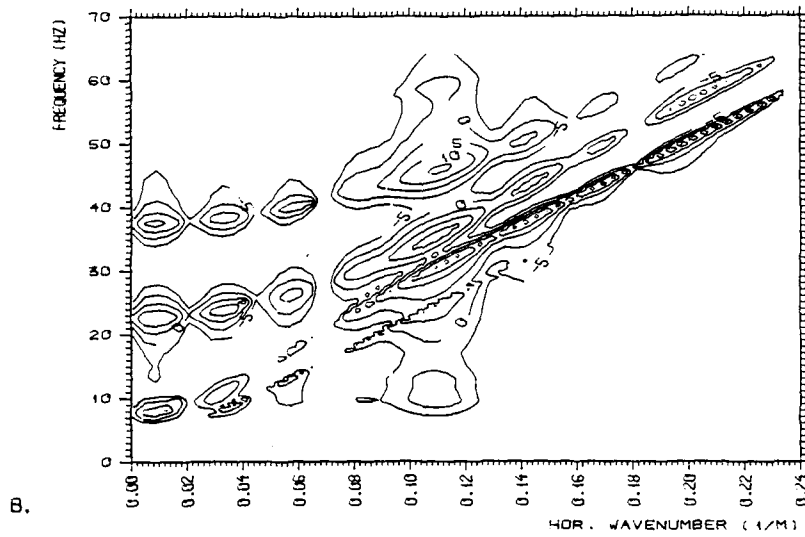


B.

Figure 3.13 Theoretical frequency-wavenumber response of the source and streamer system. A: surface plot on linear scale. B: contour plot on logarithmic scale with 5 db between contours.

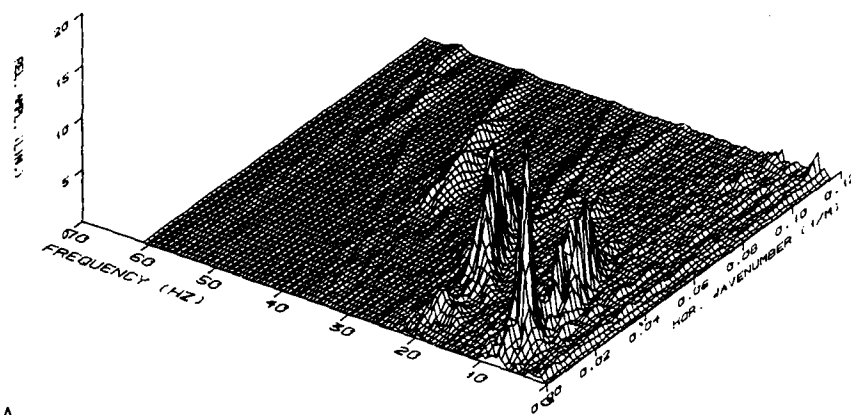


A.

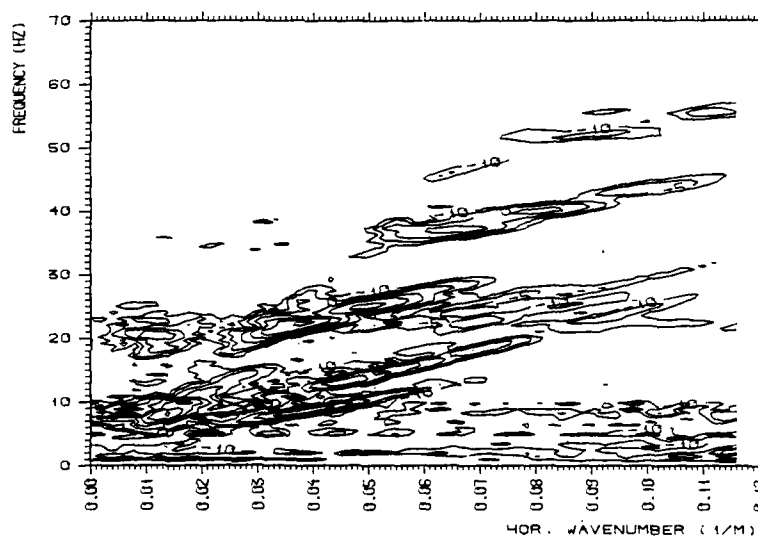


B.

Figure 3.14 F-k diagram for the same case as shown in figure 3.3 but with simulation of source- and receiver array included.
A: surface plot on linear scale, B: contour plot on logarithmic scale with 5 db between contours.

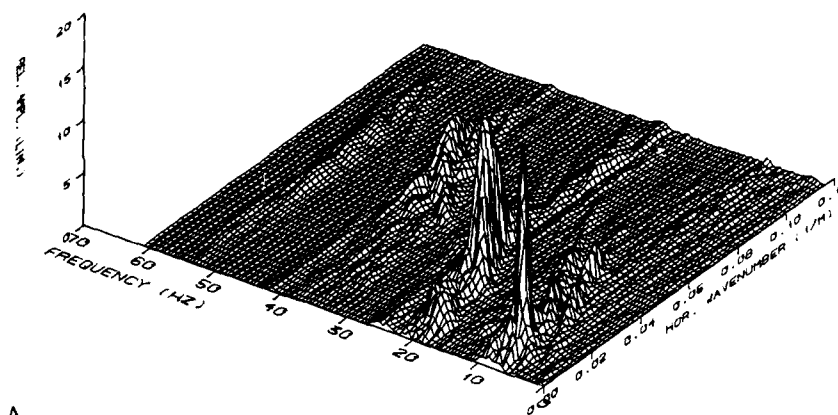


A.

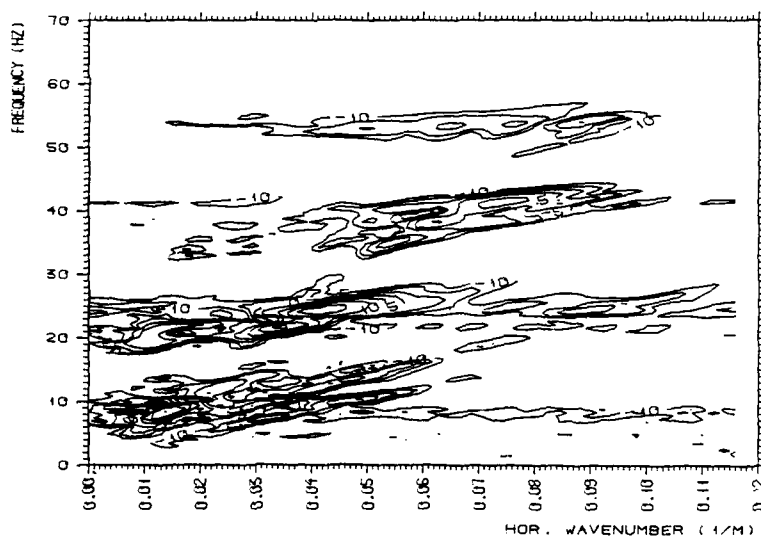


B.

Figure 3.15 F-K diagram for shot number 1. A: surface plot on linear scale. B: contour plot on logarithmic scale with 5 db between contours.

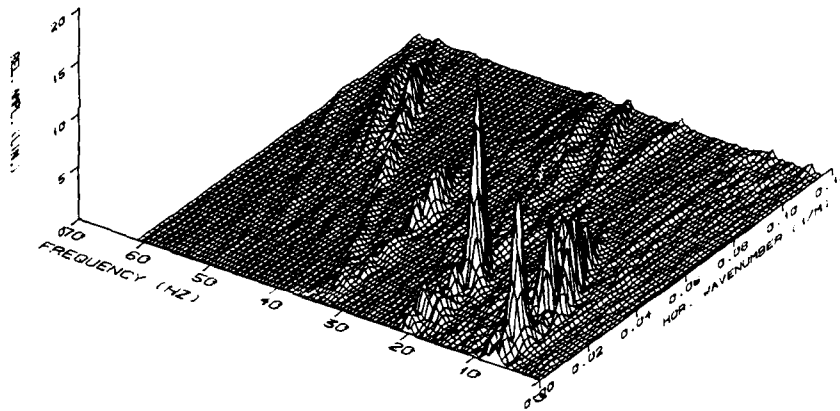


A.

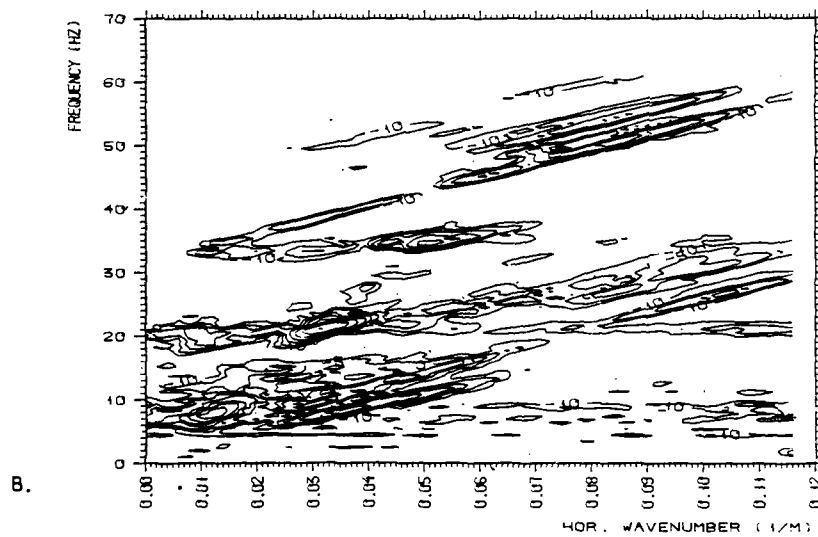


B.

Figure 3.16 F-k diagram for shot number 52. A: surface plot on linear scale. B: contour plot on logarithmic scale with 5 db between contours.



A.



B.

Figure 3.17: F-k diagram for shot number 100. A: surface plot on linear scale. B: contour plot on logarithmic scale with 5 dB between contours.

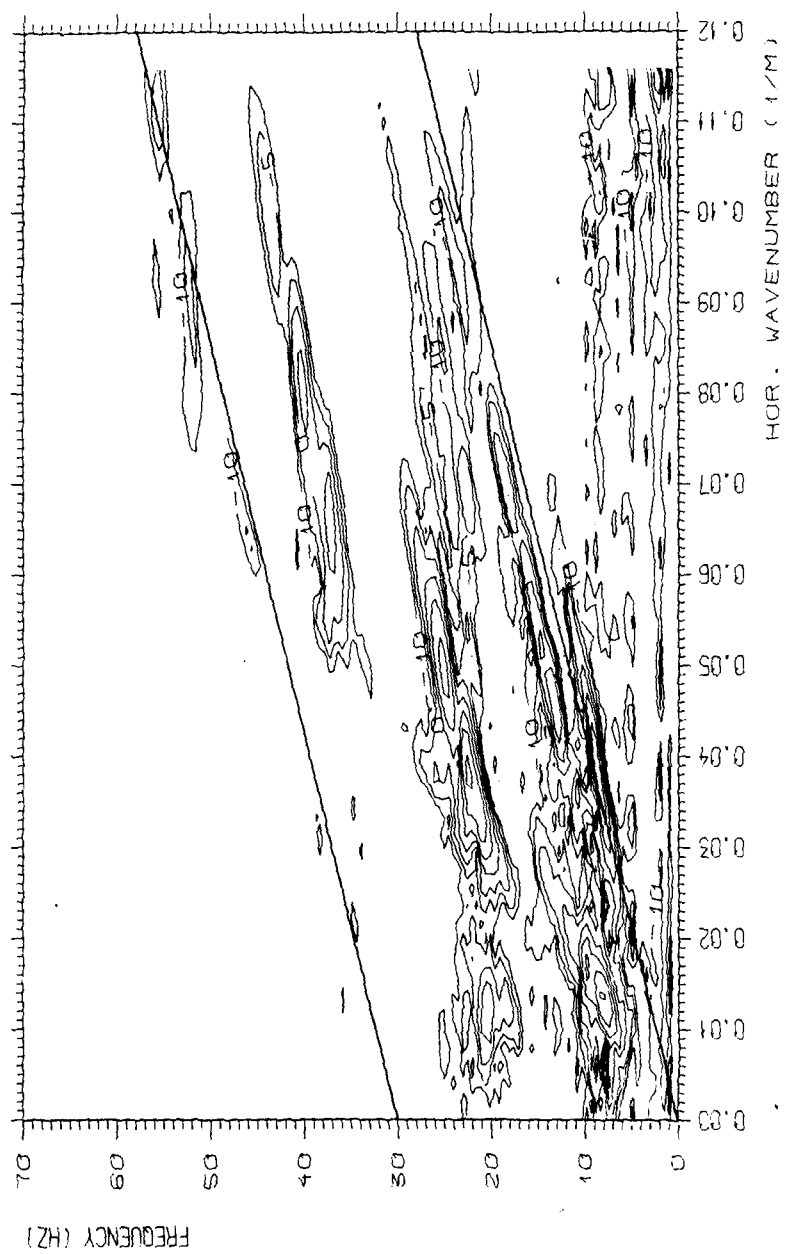


Figure 3.18 Contour plot for $f-k$ diagram for first shot. The line marker indicates a velocity of 1466 m/s.

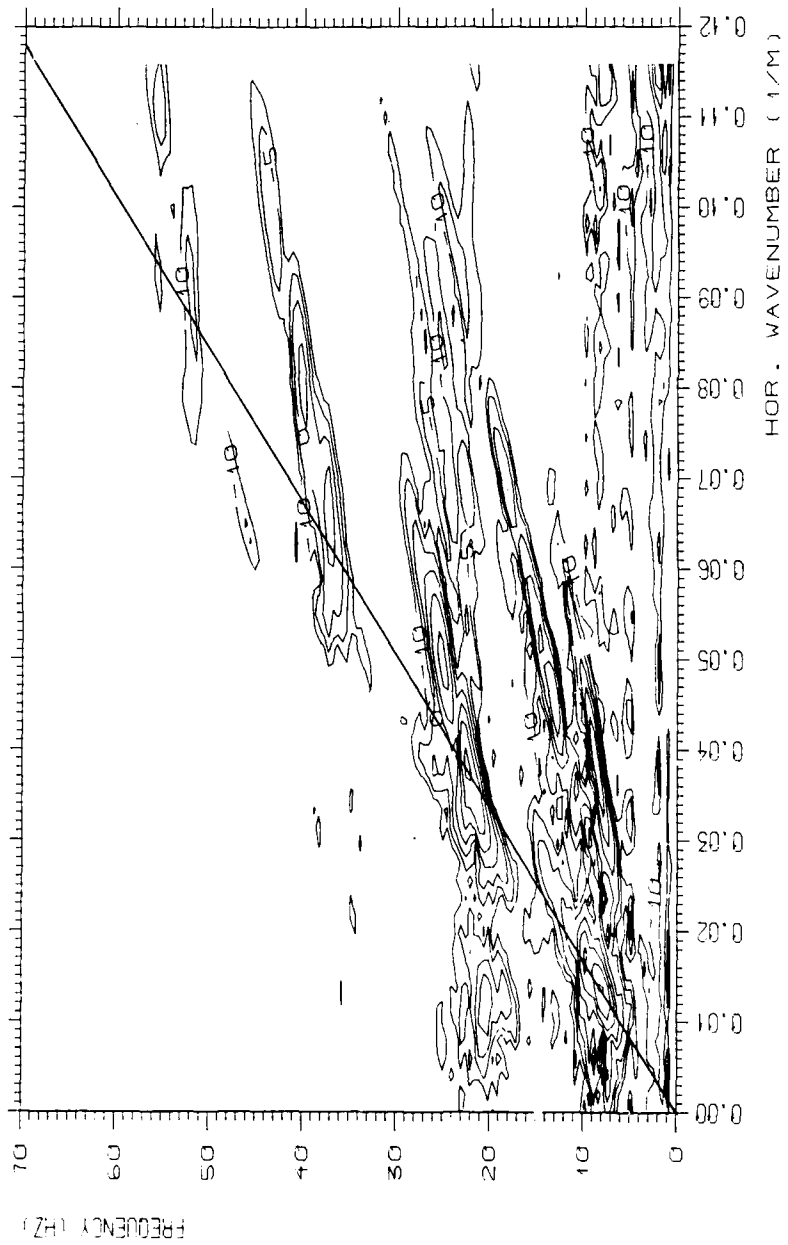


Figure 3.19 Contour plot for f-k diagram for first shot. The line marker indicates a velocity of 3700 m/s.

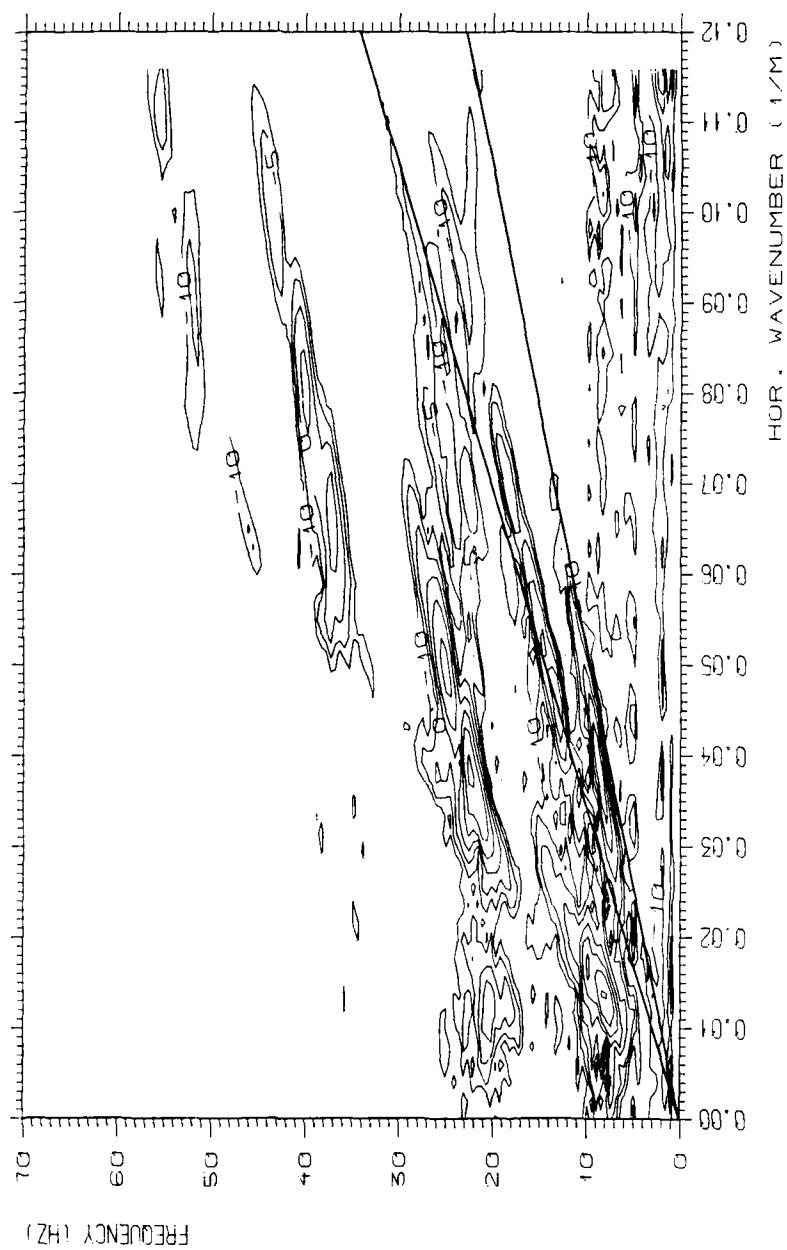


Figure 3.20 Contour plot for f-k diagram for first shot. The line markers indicate velocities of 1780 m/s and 1204 m/s.

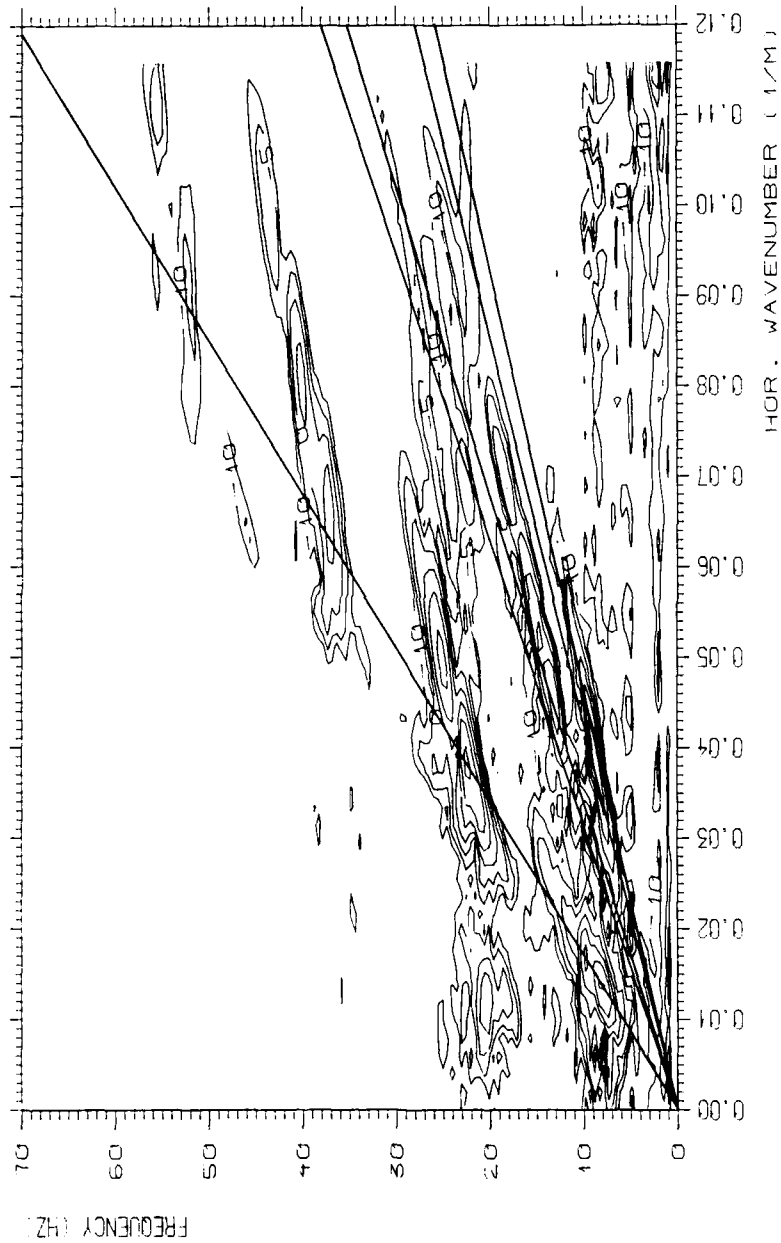


Figure 3.21 Contour plot for f-k diagram for first shot. The line markers indicate velocities of 1844 m/s, 1466 m/s and 1158 m/s.

AD-A172 754

INTERACTION BETWEEN WATER BORNE WAVES AND SEISMIC WAVES 2/2

IN THE OCEAN BOIL (U) NORWEGIAN DEFENCE RESEARCH

ESTABLISHMENT KJELLER J GLATTETRE 15 APR 86

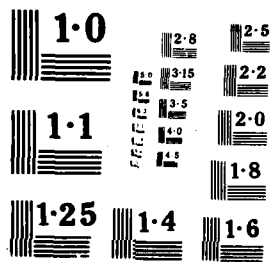
UNCLASSIFIED

NDRE/PUBL-86/1001

F/G 28/1

NL

END
DATE
FILMED
1986
DTIC



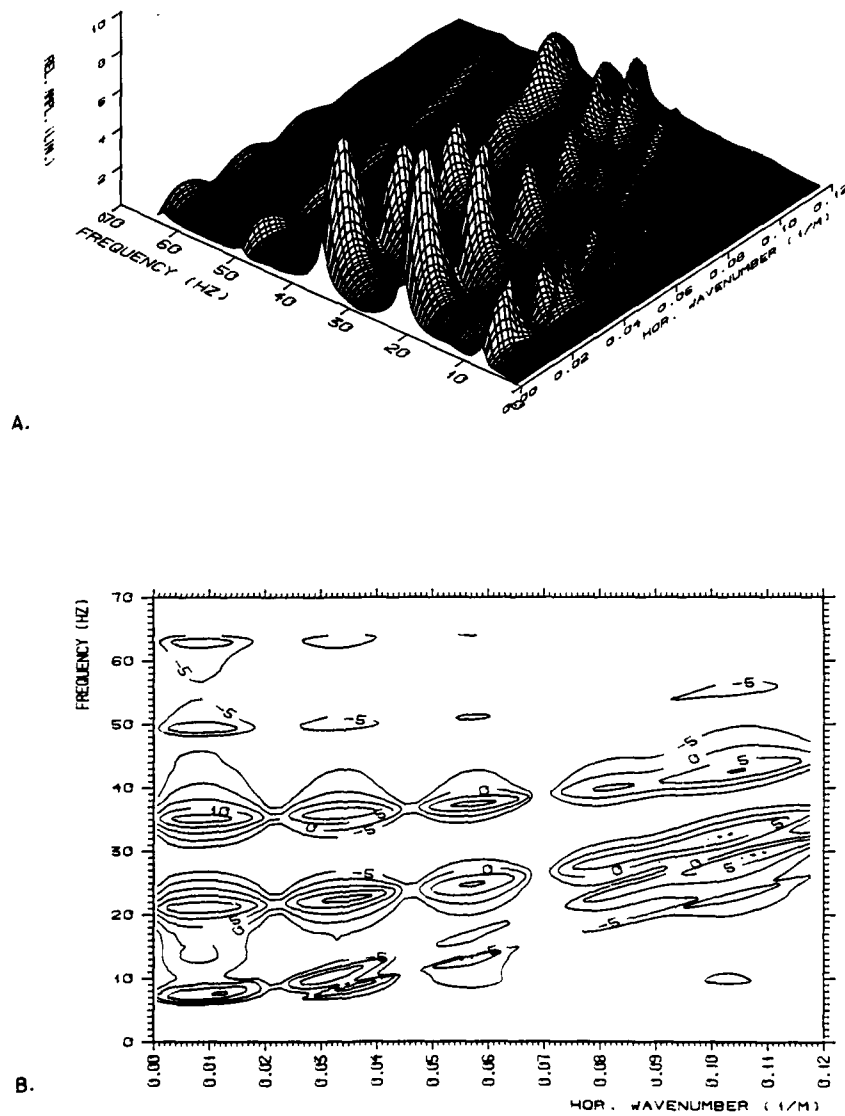
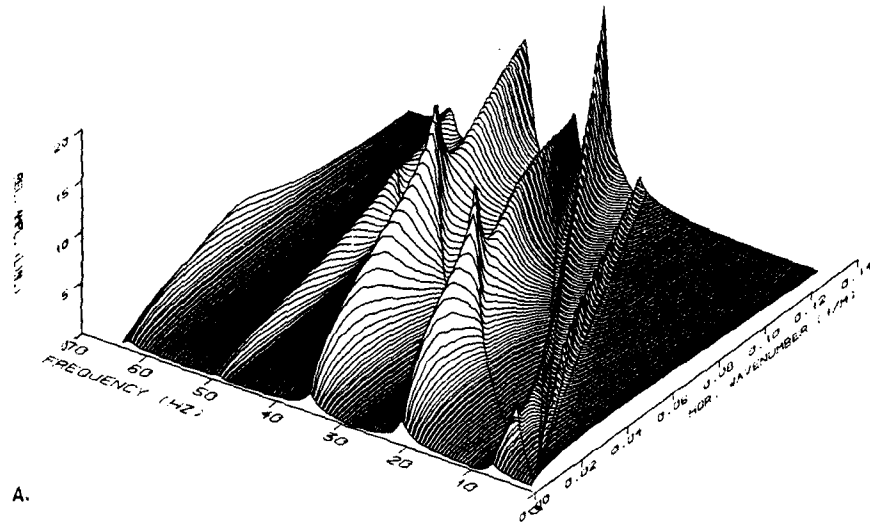
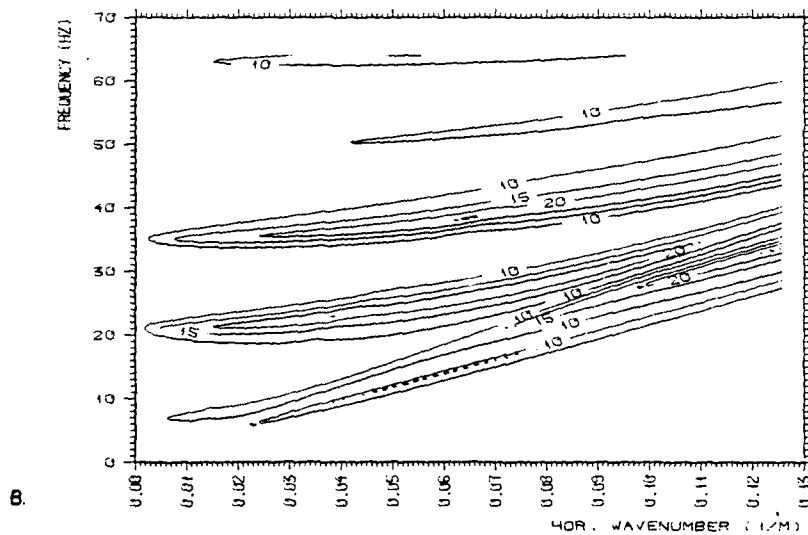


Figure 3.22 F-k diagram for 1. approximation to shot number 1. simulation of source- and streamer system is included. A: surface plot on linear scale. B: contour plot on logarithmic scale with 5 db between contours.

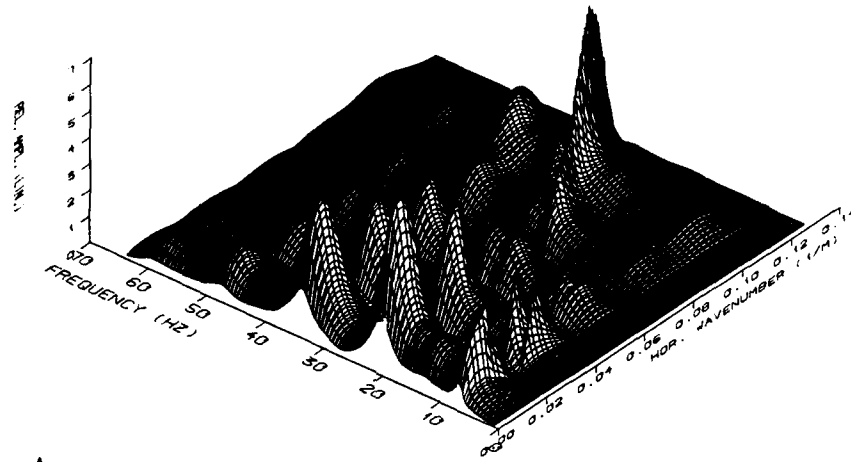


A.

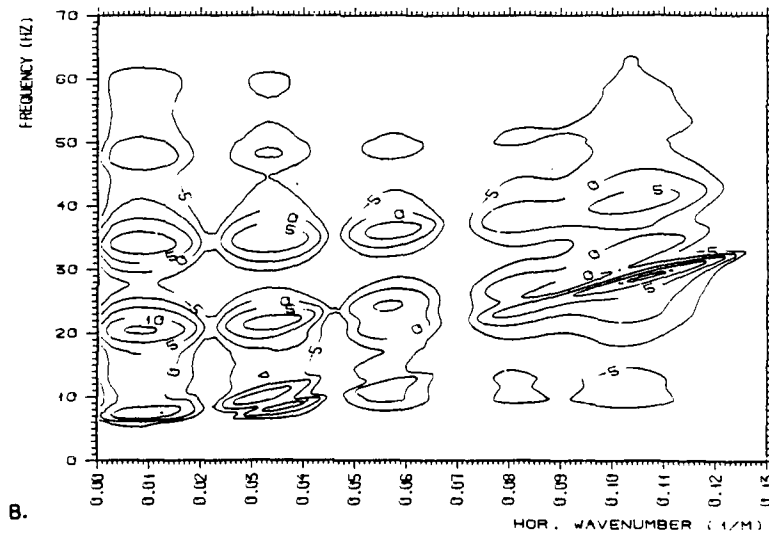


B.

Figure 3.23 F-k diagram for 1. approximation to shot number 1. simulation of source- and streamer is not included. A: surface plot on linear scale. B: contour plot on logarithmic scale with 5 db between contours. The line markers indicate velocities of 3700 m/s, 1990 m/s, 1844 m/s, 1466 m/s and 1358 m/s.

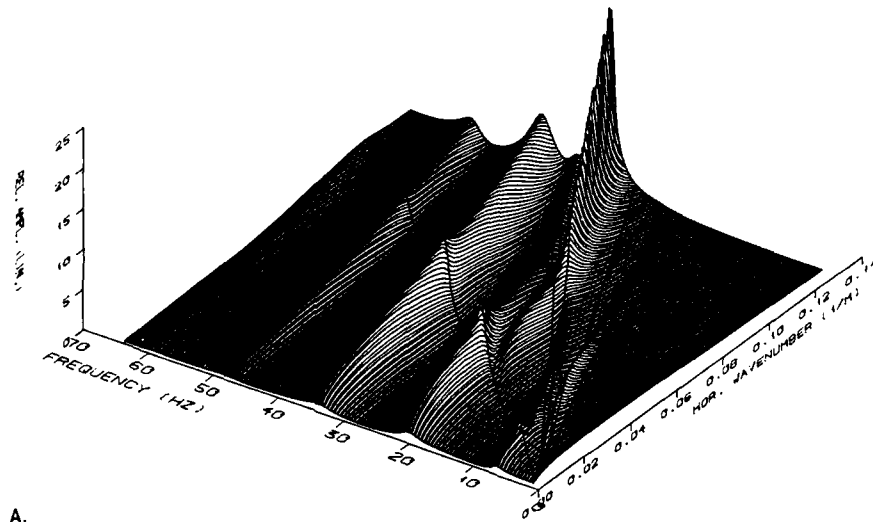


A.

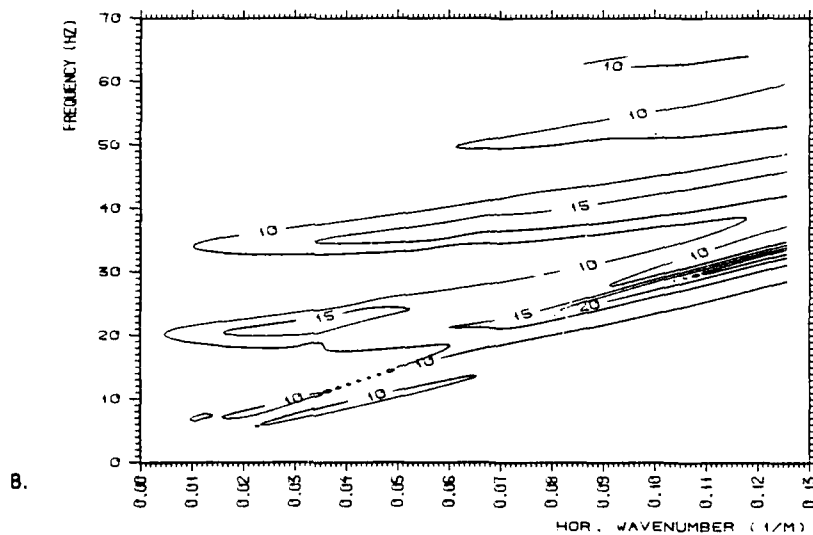


B.

Figure 3.25 F-k diagram for 2, approximation to shot number 1. Simulation of source- and streamer system is included. A: surface plot on linear scale. B: contour plot on logarithmic scale with 5 db between contours.

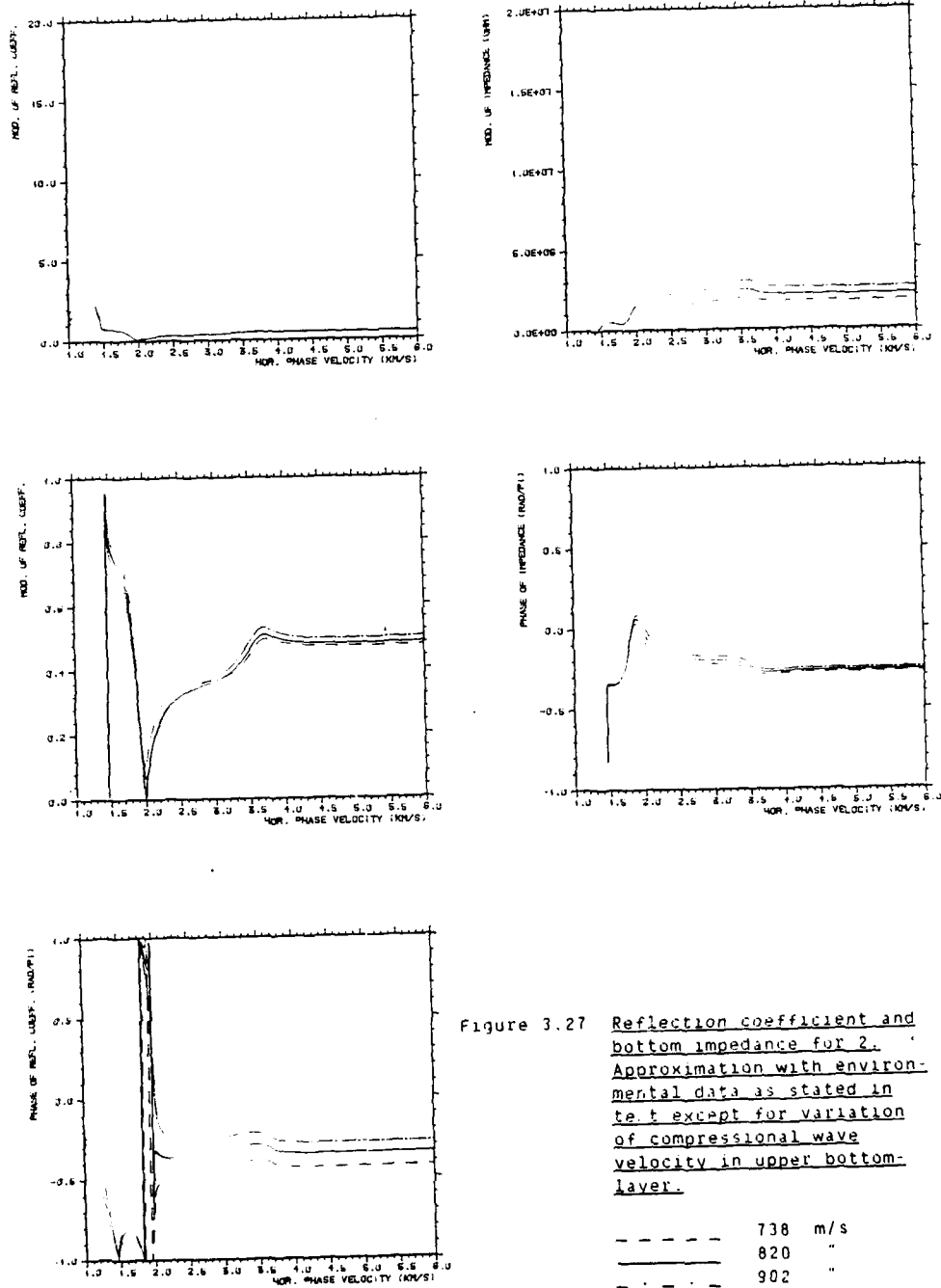


A.



B.

Figure 3.26 F-k diagram for 2. Approximation to shot number 1. Simulation of source- and streamer is not included. A: surface plot on linear scale. B: contour plot on logarithmic scale with 5 db between contours. The line markers indicate velocities of 3700 m/s, 1990 m/s, 1884 m/s, 1466 m/s and 1200 m/s.



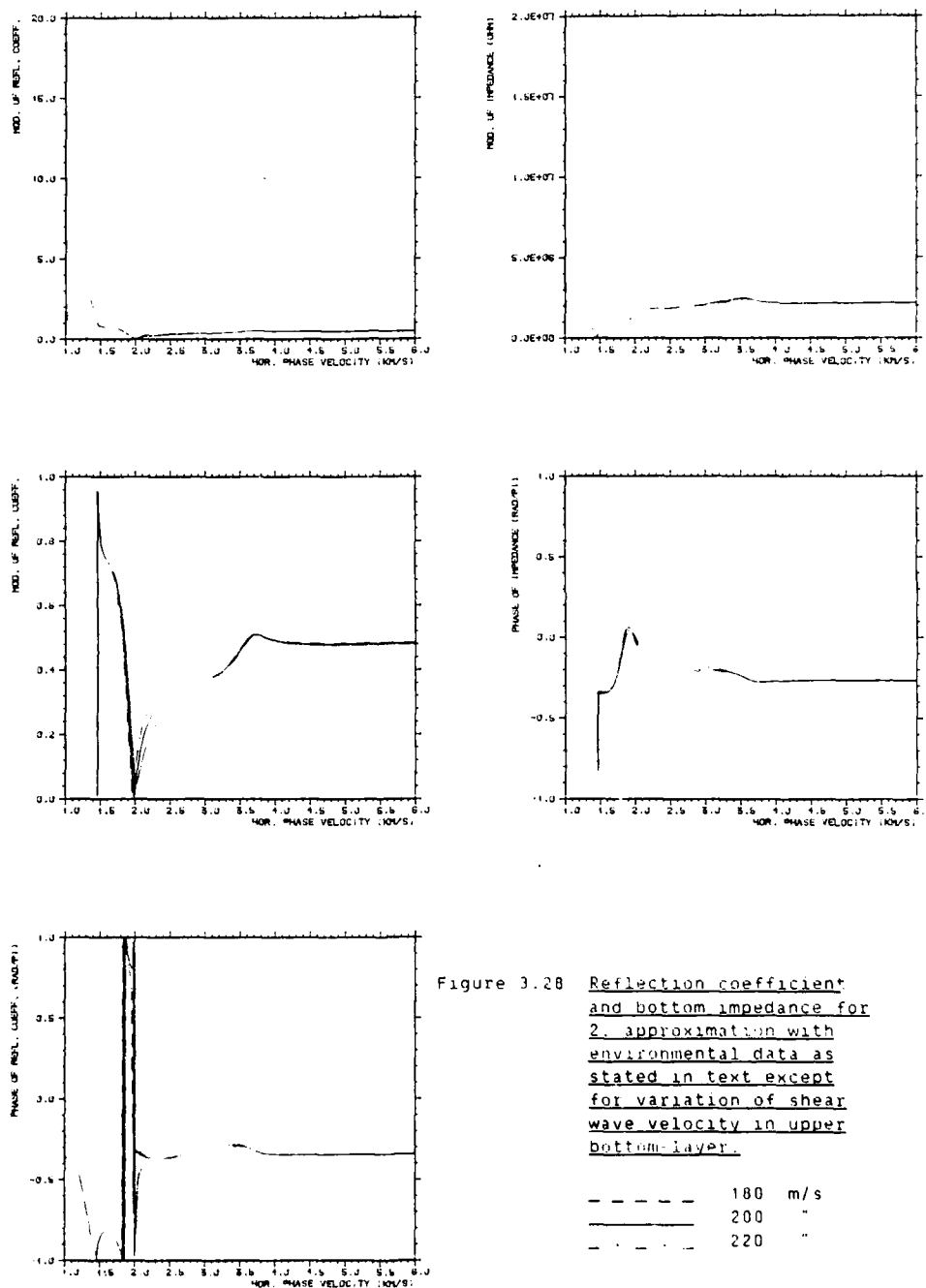
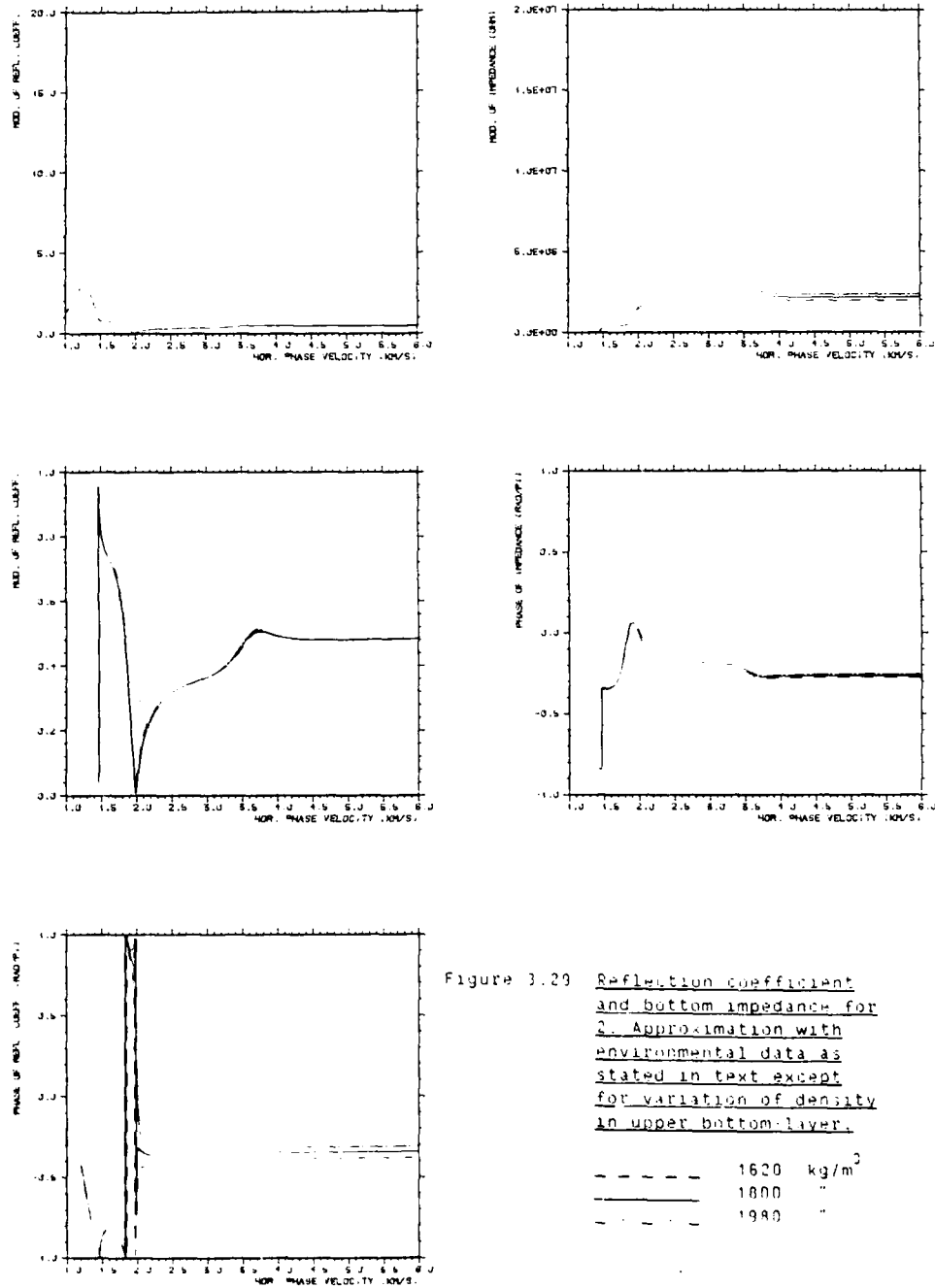
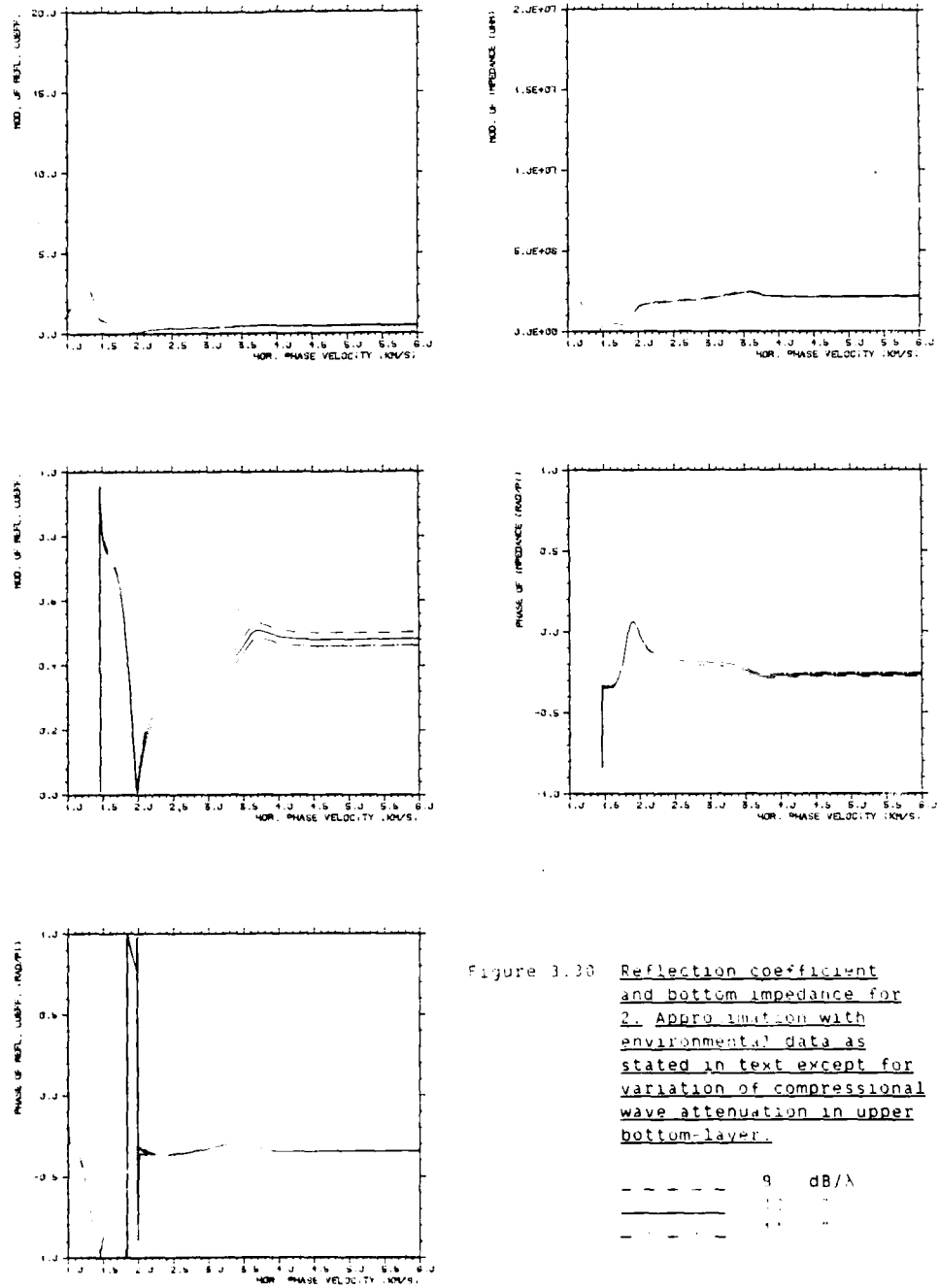


Figure 3.28 Reflection coefficient and bottom impedance for 2. approximation with environmental data as stated in text except for variation of shear wave velocity in upper bottom-layer.





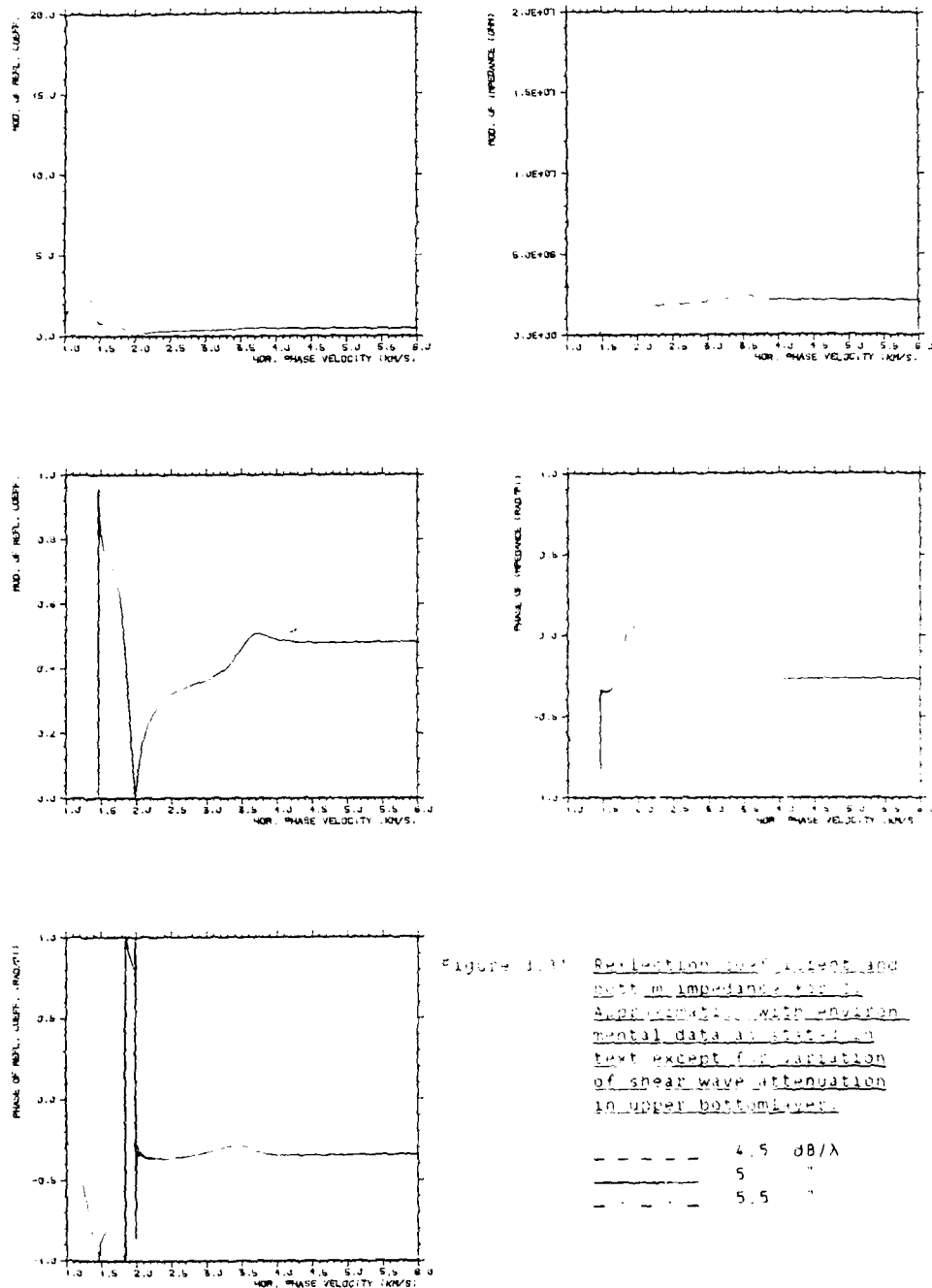


Figure 3.1: Reflection coefficient magnitude and phase versus normalized phase velocity for different bottom impedances and attenuation coefficients. The data are taken from the experimental data at 500 kHz, except for variation of shear wave attenuation in upper bottom layer.

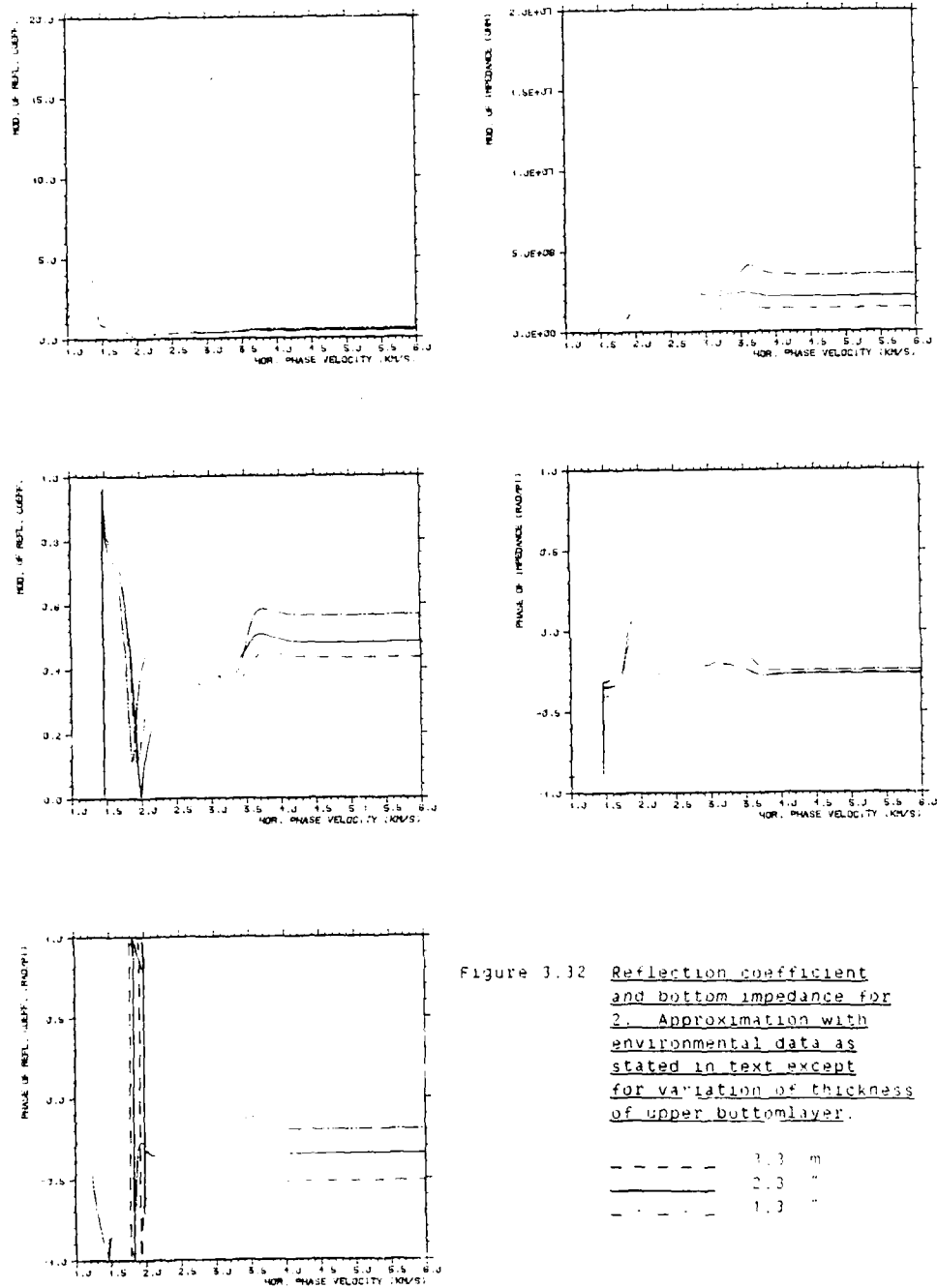


Figure 3.32 Reflection coefficient and bottom impedance for 2. Approximation with environmental data as stated in text except for variation of thickness of upper bottom layer.

END

DATE
FILMED

11 - 86

DTIC